Universidad de Concepción

Universidad de Concepción

An outflow in the Seyfert ESO 362-G18 revealed by Gemini-GMOS/IFU

(Un outflow en la Seyfert ESO 362-G18 revelado por Gemini-GMOS/IFU)

Tesis para optar al grado de Magíster en Ciencias con Mención en Física

Pedro Kurmi Humire Rodríguez

Tutor: Dr. Neil Nagar

Concepción, Chile
Agosto 2017

Agradecimientos

Es imposible resumir en estas pocas líneas los agradecimientos a quienes me ayudaron con la gran tarea de finalizar mis estudios, no sólo los de magíster, sino de los necesarios para poder vivir y plantearme la idea de estudiar astronomía. En primer lugar debo mencionar a mi familia, pues su apoyo ha sido fundamental y sin ellos quizás no hubiese podido encontrar lo que he querido ser a mis 24 años. Gracias a mi madre, de quien oí la palabra "astronomía" por primera vez y a mi padre, por su cariño sin comparación y de quien seguramente heredé la forma de ver el mundo. Gracias a mis abuelos por su gran dedicación para enseñarme las cosas fundamentales de la vida, a pesar de que ahora ya no puedan recordarlo. A mi abuelita por enseñarme a leer y a escribir cuando me enfermaba y no iba al colegio, a mi abuelo por llevarme a mi primer día de clases, acompañándome hasta los pasos finales de esta tesis, es a él a quien dedico este trabajo.

Los últimos 7 años han sido de gran aprendizaje y tengo la alegría de decir que tras ellos me he hecho de grandes amigos. Quisiera agradecer a quienes siempre ofrecieron su sincero compañerismo, como son Osvaldo Castro, Gerald Neumann, Lientur Celedón, Alex Alarcón y Bastián Reinoso. Sin ellos los espacios entre clases hubiesen sido extremadamente aburridos y, debo admitirlo, algunos aspectos de los ramos hubiesen sido ininteligibles.

Quisiera dedicarle este último párrafo a mi compañera Claudia, quien me ha dado un ejemplo de superación y ha soportado mi mal humor y falta de tiempo cuando las cosas no resultaban en esta tesis.

Abstract

It is now widely accepted that the intense radiation emitted by an active galactic nucleus (AGN) is due to accretion onto their central supermassive black hole (SMBH) in the mass range $\sim 10^6$-$10^9\,M_\odot$ [8, 62]. However, the mechanisms responsible for transferring the mass from galactic (kpc) scales down to nuclear scales (sub-parsec) to feed the SMBH are still under debate. This has been the subject of many theoretical and observational studies [27, 50, 63, 64, 97, 98, 101].

The present thesis is one more within those observational studies, where the case of the nearby Seyfert 1.5 galaxy ESO 362-G18 is investigated, analyzing the stellar and gaseous kinematics of its inner 0.7×1.2 kpc^2. While the stellar kinematics does not present interesting features more than those associated with the pure rotation of the galactic disk, the gaseous kinematics show an important additional component, well observed in the majority of the stronger emission lines which come from more volatile gases and, therefore, more likely to be altered by an external or recent factor such an outflow/inflow event. Given the nature of this component, it was quickly associated with an outflow, which is moving away from us. The kinematics could be solved, which allowed to estimate a variety of important quantities, such as the mass outflow rate, the outflow kinetic power, the total mass in the nuclear region, and that of the SMBH. Besides, previous data allowed me to determine the mass accretion rate.

My results will be very useful to increase the sample of galaxies studied kinematically in detail so far, improving the credibility of initial conditions used in simulations, looking for differences between active and inactive galaxies, etc., in an attempt to understand the evolution

of galaxies.

Resumen

Actualmente está ampliamente aceptado que la intensa radiación emitida por un núcleo activo de galaxias (AGN) se debe a la acreción sobre su agujero negro súper masivo central (SMBH) (Lynden-Bell 1969; Begelman et al. 1984) en un rango de masas $\sim 10^6$-$10^9\,M_\odot$. Sin embargo, los mecanismos responsables de transferir masa desde escalas galácticas (kpc) hasta escalas nucleares (sub-parsec) para alimentar el SMBH, están todavía en debate. Este ha sido el objetivo de muchos estudios teóricos y observacionales [27, 50, 63, 64, 97, 98, 101].

La presente tesis es uno más dentro de dichos estudios observacionales, en donde se investiga el caso de la galaxia cercana Seyfert 1.5, ESO 362-G18, analizando la cinemática estelar y gaseosa de sus 0.7×1.2 kpc^2 nucleares. Mientras la cinemática estelar no presenta características interesantes más que aquellas asociadas a la rotación del disco galáctico, la cinemática gaseosa muestra una importante componente adicional, claramente observada en la mayoría de las líneas de emisión más fuertes provenientes de gases más volátiles y, por tanto, más propensos a ser alterados por un agente externo o reciente, como un flujo hacia afuera o hacia adentro. Dada su naturaleza, esta componente fue rápidamente asociada a un flujo hacia afuera, el cual se aleja de nosotros. Se pudo resolver su cinemática, lo que permitió estimar una variedad de cantidades importantes, tales como la tasa de flujo de masa hacia afuera, la potencia cinética de dicho flujo, la masa total de la región nuclear y la del SMBH. Además, datos previos me permitieron estimar la tasa de acreción de masa.

Mis resultados serán de gran utilidad para aumentar la muestra de galaxias estudiadas cinemáticamente en detalle hasta ahora, mejorando

la credibilidad de condiciones iniciales usadas en simulaciones, buscar diferencias entre galaxias activas e inactivas, etc., en un intento por entender la evolución de galaxias.

Contents

List of Figures

List of Tables

Chapter 1

Introduction

1.1 Active Galactic Nuclei

The term Active Galactic Nuclei (AGN) refers to the existence of high energetic/non-stellar processes in the nucleus of galaxies. This nucleus is typically highly variable and very bright compared to the rest of the galaxy. It is currently though that the intense radiation emitted by an AGN is due to accretion onto a supermassive black hole (SMBH) in the mass range $\sim 10^6$-10^9 $M_\odot$ [8, 62] .

At least 45% of all galaxies in the nearby universe host an AGN [48], these galaxies are commonly called "active". There are two largest groups of AGN: quasars and Seyfert galaxies, differentiated by the amount of radiation they emit. In the case of a Seyfert, the total energy emitted by the nuclear source at optical wavelengths is comparable to the energy emitted by all of the stars in the galaxy ($\approx 10^{11}$ $L_\odot$), but in a typical quasar the nuclear source is brighter than the stars by a factor of 100 or more [83].

According with Netzer (2015) [76] an references therein, the majority of AGN include several of the following components:

- "A subparsec-rotation-dominated accretion flow that is usually referred to as an accretion disk. Optically thick disks can be geometrically thin (thin accretion disk) or thick (slim, or thick, accretion

disk). Optically thin accretion disks or flows are occasionally advection dominated. Such structures are referred to as radiatively inefficient accretion flow (RIAF), or advection-dominated accretion flow (ADAF).

- High-density, dust-free gas clouds moving at roughly Keplerian velocities at a luminosity-dependent distance of 0.01–1 pc from the BH (the broad-line region, BLR).
- An axisymmetric dusty structure with luminosity-dependent dimensions of 0.1–10 pc (the central torus).
- Lower-density, lower-velocity ionized gas (narrow-line region, NLR) extending from just outside the torus to hundreds and even thousands of parsecs along the general direction of the opening in the torus (ionization cones). Most of this gas contains dust except for very close in, in a region referred to as the coronal line region.
- A very thin molecular maser disk similar in size to the torus.
- A central radio jet occasionally associated with γ-ray emission."

Below is shown a scheme with the mentioned AGN's regions

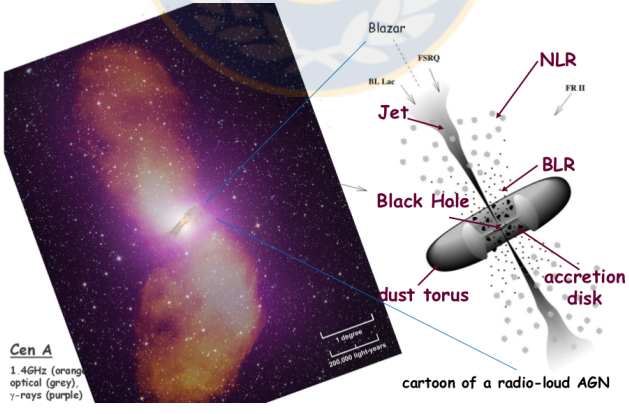

Figure 1.1: Centaurus A, scheme versus reality (Modified from Anita Reimer's slide, 5th Fermi Symposium).

1.1.1 AGN Classification and H II regions

To date, many types of AGNs have been distinguished. The mass of their SMBH range between $10^5 M_\odot$ [85] and $10^{10} M_\odot$ [116] and their bolometric luminosity L_{bol} range from 10^{41} to 10^{48} erg s^{-1}.

In 1943, Carl Seyfert discovered high redshifted and very luminous spiral galaxies, now called Seyfert galaxies; but his work was not very considered until 1960s, when strong radio sources were discovered with optical counterparts often appeared point-like, leading to the designation of "quasi-stellar objects" (QSOs) for those. Nowadays, the distinction between Seyferts and QSOs does not exist [83] and was due in its beginnings to the great difference between luminosities and redshifts observed in those times. However, with the development of new instruments, more objects have been found binding the gap. Below is present a summary of some AGN types and H II regions. For a review, see Tadhunter (2008) [108].

- H II regions: Are regions whose emission line spectra is produced by massive gas clouds of ionized hydrogen. They are detected mostly in spiral, irregular and compact galaxies and always present strong forbidden oxygen lines with [O III] λ5007 Å/H$\beta > 3$. These objects typically present electron temperatures in the range 5.000 – 18.000 K with the cooler objects showing higher abundances of heavy elements. Electron densities are usually of the order of few dozen to a few hundred per cm^{-3}. Unlike AGNs, the ionizing sources are massive O and B stars embedded in star-forming regions instead an accreting SMBH.

- Seyfert Galaxies: The distinction between Seyfert and non-active galaxies is the bright, central, point-like core, with the optical spectra dominated by high-excitation nuclear emission lines which can show both broad (>1000 km s^{-1}) and narrow (few 100 km s^{-1}) emission lines or only narrow emission lines. The first are called Seyfert 1 galaxies and the second, Seyfert 2 galaxies. Based on the strength in the broad component of Hβ, intermediate objects have been classified as Seyfert 1.2, 1.5, 1.8 and 1.9, following the scheme introduced by Osterbrock (1977) [78]. Besides, a subset of

Seyfert 1 galaxies, called narrow-emission line Seyfert 1 galaxies (NLS1) present broad Hα lines but narrow Hβ (FWHM Hβ < 2000 km s^{-1}) similarly as in Seyfert 1.9 [81].

- LINERs: The low-luminosity nuclear emission-line regions (LINERs), as part of the called low luminosity AGNs (LLAGNs) class; are objects that show faint nuclear luminosities and strong emission lines originating from low ionized gas. It remains uncertain whether all LINERs are truly AGNs, or rather a subset of them represent nuclear star-forming regions [44]. If the former is true and considering transition objects with a LINER component, LINERs constitute the dominant population of AGNs: 33% of all galaxies and 66% of AGNs [43]. Line widths are usually of 200 – 400 km s^{-1} and their properties are very similar to Seyfert 2 galaxies but with stronger forbidden lines and can show [O III]λ5007Å/Hβ < 3. In comparison to H II regions, LINERs have stronger [N II] lines than Hα line flux. The X-ray spectra are dominated by starburst emission rather than by the AGN core.

  A list with other AGN classifications according with the unified scheme (Sect. 1.1.2) and some observable features are present in Table 1.1.

In 1981, Baldwin, Phillips and Terlevich published some diagnostic diagrams, of which the most useful to date has been the called "BPT diagram" [6]. This diagram use four strong emission lines in the optical wavelength range to distinguish between AGN (Seyfert, LINERs) and star-forming dominated galaxies (H II regions). The choice of such lines allows to avoid contamination by redshift since they are so close in wavelength: Hα λ6563 Å with [N II]λ6583 Å and Hβ λ4861 Å with [O III] λ5007 Å. Several adjustments have been proposed for this diagram due to the absence or difficulties in obtain some required emission lines [17] or extreme nature in the interstellar medium of galaxies at high redshift (z $\geqslant$ 1.5) [49].

Although the different AGN types mostly occupy separated regions in the BPT diagram, in some cases this gives rise to ambiguities of classification. That is why other line ratios (Figure 1.3) have also been considerer, such as [S II] and [O I] emission lines.

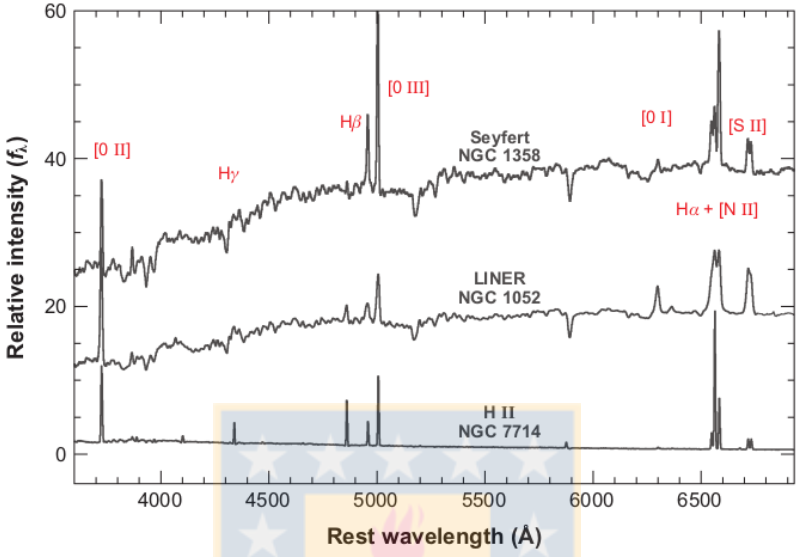

Figure 1.2: Seyfert, LINER and H II spectra: optical sample of various classes of emission-line nuclei and H II regions. Prominent emission lines are labeled. From Ho (2008) [43].

1.1.2 AGN Unified Model

The *general* AGN unification model proposes that the large diversity of observed AGN properties can be explained by the torus inclination to the line-of-sight (LOS), if the AGN produces jets and the source luminosity. For example, the existence of an optically thick torus surrounding the central regions of an AGN on scales of 1-100 pc would lead to absence of broad emission lines in the case of Seyfert 2 if they are observed edge-on, because the broad line region would be hidden, while Seyfert 1 are mostly observed face-on [4, 33]. An scheme of this unified model is present in Figure 1.4.

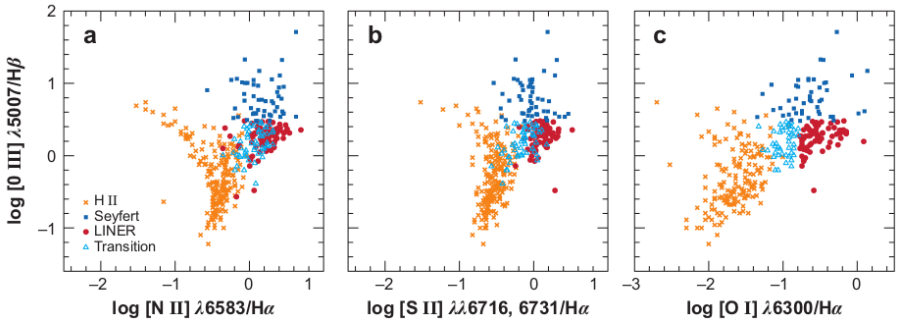

Figure 1.3: Diagnostic diagrams, (a) log [O III]λ5007Å/Hβ versus log [N II]λ6583Å/Hα, (b) log [O III]λ5007Å/Hβ versus log [S II]λ6731Å/H, and (c) log [O III]λ5007/Hβ versus log [S II]λ6300/Hα. From Ho (2008) [43].

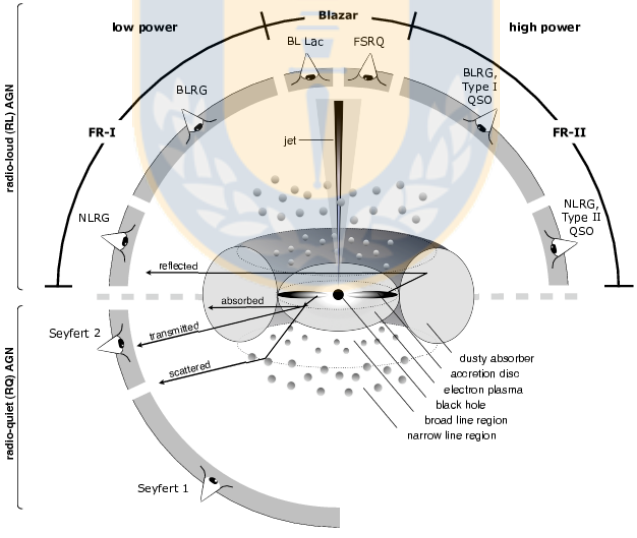

Figure 1.4: AGN unification scheme. The type of object that is seen depends on the viewing angle, if the AGN produces jets and the power of the central engine. Graphic by Marie-Luise Menzel (see e.g. https://arxiv.org/pdf/1302.1397). From https://inspirehep.net/record/1217833/plots.

Table 1.1: Features of different types of galaxies, according with the unified scheme of AGN and considering various observable parameters. From the book by Beckmann, V., & Shrader, C. 2012, Active Galactic Nuclei.

Radio loud?	AGN type	Subtype	X-ray absorbed? $N_H > 10^{22}$ cm^{-2}	Broad Balmer lines?	Narrow Balmer lines?	Fe$K\alpha$	γ-rays?
RL							
	Radio galaxy						
		WLRG	Yes	Yes	Yes	No	No
		BLRG	No	Yes	Yes	Yes	Few
		FR I/II	No	Some	Yes	No	No
	Quasar	Type 1	No	Yes	Yes	Yes	Some
	Quasar	Type 2	Yes	No	Yes	Yes	No
	Blazar						
		FSRQ	No	Yes	Yes	Some	Yes
		BL Lacs	No	No	No	No	Yes
RQ							
	Seyfert 1		$< 10\%$	Yes	Yes	Yes	No
	Seyfert 1.5		$\sim 30\%$	Yes	Yes	Yes	No
	Seyfert 2		$> 90\%$	No	Yes	Yes	No
	NLS1		$< 10\%$	Yes	Yes	Yes	Few
	ULIRGs		Yes	Yes	Yes	No	No
	LINER		Yes	No	Yes	Yes	No

Early arguments were made in favor of this model, specially since the discover of emission lines from the broad line region in Seyfert 2 galaxies by using spectropolarimetry (e.g. NGC 1068, Antonucci & Miller (1985) [5]): If the emission lines from the BLR are actually hidden by the torus in Seyferts 2, then some percentage of their light is scatter to the line-of-sight by dust grains and free electrons above and below the disk, and this light contains broad Balmer lines. Besides, it was found that the percentage of these emission lines from the BLR is related with the galactic inclination, according with the unified model. However later and deeper polarimetry [109] shows a large fraction of Seyferts 2 (approximately half of the total currently known population) with no hint of polarized broad Hα lines (the most prominent). While other explanations, such as Compton thick obscurers, have been proposed, it seems that many of such objects are unobscured but void of BLR gas.

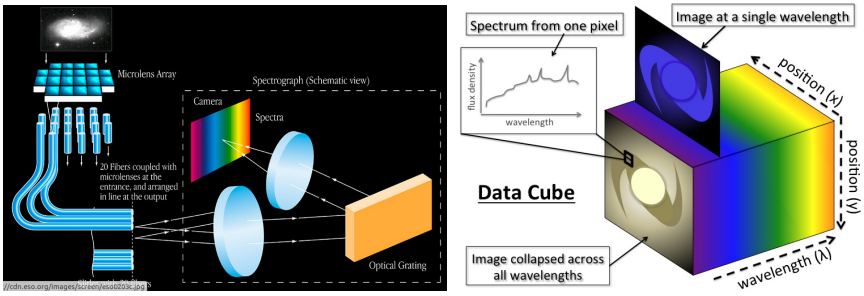

Figure 1.5: Integral field Spectrograph and data cube schemes, from left to right, respectively. From ESO Chile (left panel, https://www.eso.org/public/chile/teles-instr/technology/ifu/) and Harrison thesis (right panel, http://astro.dur.ac.uk/ cpnc25/research.html).

1.1.3 Kinematics and dynamics of Galaxies through IFS

To better understand the evolution of galaxies, it is vitally important to observe the kinematic processes that occur in them, from their outer regions down to the regions surrounding the nuclear supermassive black hole. For this is necessary a panoramic view of what is happening, something never better achieved than through the Integral Field Spectroscopy (IFS). In this method, the signal from each cell or spatial pixel (spaxel) of the field of interest in the sky is fed into a spectrograph equipped with an integral field unit (IFU), which then generates a spectrum for each individual spaxel. All the resulting spectra are arranged into a datacube which contains the entire 2D field of view plus the third dimension drawn from the spectrograph. In Figure 1.5 a couple of schemes showing the observing process of an IFS (left) and the resulting data cube (right). Early works that provided in optical wavelength, two-dimensional gas kinematic maps of the central parts in nearby active galaxies have been, for example, NGC 3227 [68] and NGC 1068 [35] and, in the near-infrared (NIR), the Circinus galaxy observed with the NACO spectrograph and SINFONI at the Very Large Telescope [71] and NGC 3227 [23] observed with SINFONI.

It is known that stars can only change their velocities in a continu-

ous manner, by acceleration due to the gravity and that, having a small density, do not interact mostly during a merger of galaxies. Then, stellar kinematics can give us a direct information about the gravitational potential in galaxies and information of how they were before a merger event.

In galaxies outside the immediate surrounding of the Milky Way, where the light of a single star is impossible to resolve, the line-of-sight velocity distribution (LOSVD), which is the probability to find a star in a specific point of the galaxy with a certain projected velocity, contains all the possible information. Then, to measure the stellar kinematics it is required to assume that what is seen in an specific galactic spectra is the sum of all contribution of stars inside the spatial resolution and along the line-of-sight. For the case of distant galaxies, contribution of other galaxies or even a cluster of them have been observed contaminating the original spectrum. The galaxy of this research, ESO 362-G18, is in the local universe ($z = 0.012445$), so those contribution can be discarded.

One good way to obtain the stellar kinematic in a galaxy is to convolve stellar or galaxy templates to the observed spectra, expanding the LOSVD as Gauss-Hermite series [36, 113]:

$$\mathcal{L}(\nu) = \frac{e^{-(1/2)y^2}}{\sigma\sqrt{2\pi}}\left[1 + \sum_{m=3}^{M} h_m H_m(y)\right]$$

where $y = (\nu - V)/\sigma$, H_m are the Hermite polynomials and h_m are the Hermite coefficients of which the first are kinematically important (h_3 and h_4, see below). Finally, the radial velocity, velocity dispersion and other stellar parameters are fitted simultaneously, following the procedure of the Penalized Pixel technique (pPXF, [16]).

On the other hand, the interstellar gas constitutes a big fraction of the interstellar medium (more than 95% total mass it) and although it is very dilute (1 atom per cm^3) is more susceptible to disturbance. Observation of neutral hydrogen (H I), for example, are useful to study large-scale interstellar medium kinematics, dark matter, effects of interaction between galaxies, and perturbations in the gravitational potential [12, 103, 112], while high ionization gas like [O III] are more volatile and can more accurately trace kinematic perturbations coming from, e.g.,

explosions of super nova or from the AGN and/or inflowing material in a galactic bar, spiral arms or a combination of both.

It is possible to extract information of the gaseous kinematics by using different approaches to its spectra features (emission lines), of which the most used is the Gaussian profile. The area under the Gaussian correspond to the integrated flux, the wavelength of the Gaussian peak is transformed in the observed velocity using the doppler effect, the width depict the velocity dispersion and, when the resolution is enough, it is also possible to measure inhomogeneities between the Gaussian fit and the real spectra such as the skewness (asymmetry) and kurtosis (degree of peakedness). All these measurements are also known as kinematic moments, where the flux is the moment 0, the radial velocity (v) is the moment 1, the velocity dispersion (σ) is the moment 2; and the skewness and kurtosis are the h_3 and h_4 Gauss-Hermite moments, respectively. For a more detailed explanation of the Gauss-Hermite moments in the kinematic context see, e.g., Riffel (2010) [88].

In order to interpret the observed velocities in an spiral galaxy, it must be assumed that they come from a single inclined plane and its rotation is the dominant pattern. With coordinates R and θ representing the radius and the azimuth angle of the major axis (the intersection between the plane of the sky and the galactic plane), respectively and an inclination i of the galactic plane. The observed velocities are:

$$V_{obs} = V_{sys} + V(R)sin(i)cos(\theta)$$

Putting these velocities versus their radial distance along a fixed axis, a rotation curve is constructed. If these velocities are seen in two dimensions, covering an area in a galaxy and not just a specific axis through it, with contours that mark the regions where the velocities are constant, the result is a contour diagram, better known as spider diagram. In Figure 1.6 two examples (models) of rotation curves (up) and their corresponding spider diagrams (bottom) are present. On the left rotation curve the velocities increase indefinitely, while in the right rotation curve the velocities begin to decrease at a radius of ~ 3, this generate circles in the spider diagram.

The kinematic measurements allow possible construct position velocity maps, structure maps, velocity fields or maps from all available

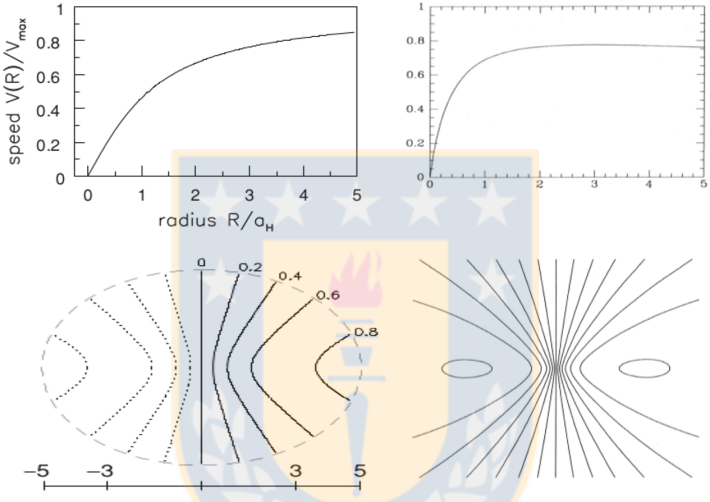

Figure 1.6: Rotation curves and spider diagrams examples: Rotation curves (up) and their corresponding spider diagrams (bottom). The velocities are normalized and the radius are divided by a constant number, a_H. Left panels are from Fig. 5.19 of the book "Galaxies in the Universe" by L. Sparke and J. Gallagher (2007). Right panels are from Paz Agüero's thesis "Cinemática y dinámica de galaxias espirales" (2010) [2].

and credible moments in addition to improvement techniques like the Voronoi binning method [15] which allows to fix a minimal signal-to-noise ratio to the measurements. With the use of velocity fields, for example, it is possible measure the level of perturbation in the kinematics like changes in the gaseous kinematic major axis along different distances from the nucleus and then compare it with the stellar kinematics to look for differences between active and non-active galaxies [26]. Also it is possible to distinguish perturbations due to bars and spirals and use these results to improve hydrodynamic models.

Bars represent an efficient way to drag material to the inner ~ 100 parsec of galaxies. However, when this material crosses the inner Lindblad resonance (ILR), the inflow is stopped and the gas is redistributed along the ILR ring. Indeed, the presence of bars alone could not be directly related to an increase in the accretion onto the SMBH and then with the activity in AGNs, and are observed with almost the same frequency in both active and non-active galaxies [50]. The presence of additional inner bars or spirals could allow a renewed inflow of material within the ILR. Observational and theoretical studies are being carried out to verify this assumption. Recent hydrodynamic models suggest that spirals induced from strong bars can fuel the SMBH with accretion rates up to 0.03 $M_{\odot}yr^{-1}$ [64], enough to power AGNs and generally above the amounts inferred from bolometric luminosities in nearby active galaxies (see table 1.2).

To give a more concrete idea of bar kinematics perturbations, in Fig. 1.7 is presented the velocity field of NGC 3227 from Davies et al. (2014) [22] along with their better fit obtained from hydrodynamical models realized by Maciejewski (2004) [64].

1.1.4 Inflows

Not just bars, but non-axisymmetric potentials in general are an efficient way to promote gas inflow towards the inner regions of galaxies [29]. Close encounters and galactic mergers have also been identified as a mechanism capable of driving gas from tens of kiloparsecs down to a few kpc [25, 42], the latter (only major mergers) are likely the only mechanism capable of triggering the most luminous AGNs [110]. Sim-

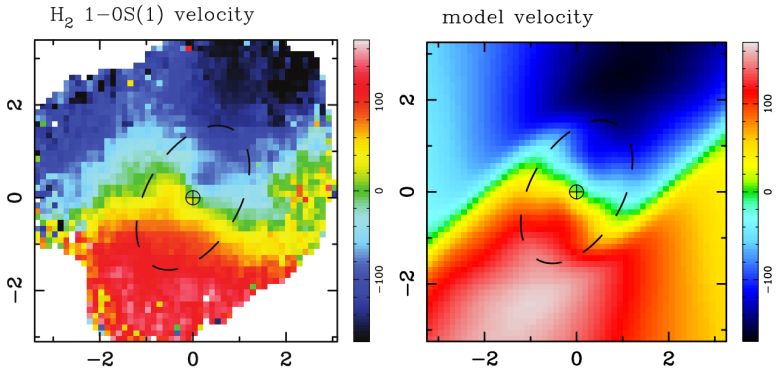

Figure 1.7: Observation and a model of a bar in NGC 3227. The observed velocity field from molecular gas (left) and the hydrodynamic model of a disk with an internal spiral generated by a large-scale bar in NGC 3227 (right) are shown. The ellipse denote a circumnuclear ring inclined with the assumed inclination of NGC 3227. From Davies et al. (2014) [22].

ulations by Hopkins and Quataert (2010) [46] suggest that in gas-rich systems, at scales of 10 to 100 pc, inflows are achieved through a system of gravitational instabilities over a wide range of morphologies such as nuclear spirals, bars, rings, barred rings, clumpy disks, and streams.

Indeed, several observations support the hypothesis that large-scale bars channel the gas to the centers of galaxies [20]. Recent studies conclude that there is an excess of bars among Seyfert galaxies as compared to non-active ones: about 75% vs. 57%, respectively [51, 54, 56]. Further, structures like disks or small scale nuclear bars and the associated spiral arms are often found in the inner kpc of active galaxies [18, 30, 55, 84]. In general, the most common nuclear structures are dusty spirals, estimated to reside in more than half of active and inactive galaxies (71% and 61%, respectively [67]).

In addition to all the above, Simões Lopes et al. (2007) [102] reported a marked difference in the dust and gas content of early-type active and non-active galaxies: the former always have dusty structures, and only 25% of the latter ones have such structures. Thus, a reservoir of gas and dust is required for the nuclear activity suggesting that the dusty

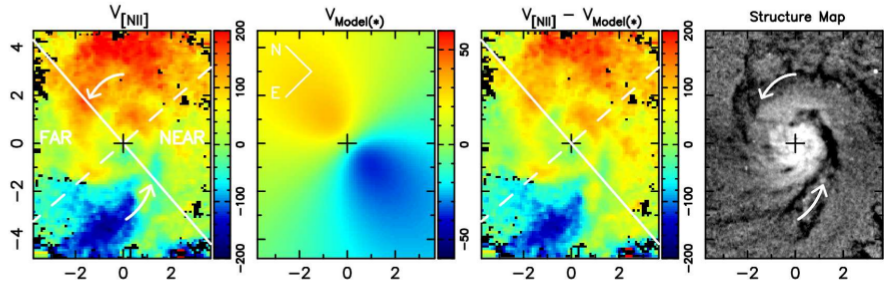

Figure 1.8: Inflowing gas in NGC 7213. From left to right: Gaseous velocity field (km s^{-1}) of the [N II] emission line, stellar rotation model, residuals between the two, and the structure map. Arrows denote the spiral arms, thought to be the pathway of the inflowing material. From Schnorr-Müller et al. (2014) [98].

structures are tracers of feeding channels to the AGN. This fact, along with the enhanced frequency of dusty spirals, supports the hypothesis that nuclear spirals are a mechanism for fueling the SMBH, transporting the gas from kiloparsec scales down to a few tens of parsecs of the nucleus.

In recent years, integral field spectroscopy of nearby AGNs has provided a clear view of the AGN processes responsible for fuelling on scales in the range $\sim$ 10–100 pc, revealing kinematical features consistent with gas inflowing towards the nucleus approximately along dusty spiral arms observed in Hubble Space Telescope (HST imaging). Examples include the case of NGC 1097 [32], NGC 6951 [105], NGC 7213 [98] and M81 [99] in the optical; for the latter, the stellar kinematics was also obtained. In the near-IR, inflows have been observed in, e.g., NGC 4051 [91] , NGC 4151 [106]; Mrk 1066 [89] and Mrk 79 [90]. A clear evidence of inflowing material along dusty spiral arms in NGC 7213 by Schnorr-Müller et al. (2014) [98] is presented in Fig. 1.8.

1.1.5 Outflows

Accretion onto the SMBH requires removal of angular momentum, which can be achieved not only through gravitational torques, but also via

outflows or winds [14], the most powerful of which are produced by the interaction between the ionized gas and the magnetic field [11] reaching velocities of up to 1000 km s^{-1} [39, 94] and outflow rates several times larger than host galaxy star formation rates [107]. Massive AGN-driven outflows have been observed in many AGN, from Seyfert galaxies to quasars, at low [69] and high redshifts [75], and could dramatically affect the evolution of galaxies due to the large amounts of energy they feed back into the interstellar medium [25].

Outflows in AGNs at kpc scales has beed studied for more than 30 years (for an early review, see Bridle & Perly (1984) [14]). Radio images showing jets and lobes associated with the AGN are a clear evidence that these objects are capable of eject material from their energetic nuclei at relativistic speeds [13].

At the less powerful end, studies of nearby Seyferts show that compact outflows ($\sim$100 pc in extent) with velocities of $\sim$100 km s^{-1} and mass outflow rates of a few solar masses per year are common in low-luminosity AGNs [e.g., 22, 72]. At these low outflow velocities it can be difficult to disentangle if AGNs or host galaxy starburts are responsible for the outflow. A cutoff of 400–500 km s^{-1} is often used [77] to differentiate the two, since that velocity requires $\sim$ 1 keV per particle, something difficult to achieve with stellar processes in large masses of cold molecular gas [31] and, therefore, can only be due to a powerful AGN in the center of the galaxy. For this purpose emission lines of high ionization (also called corona lines) can be used, since they are free of potential star formation contributions, thus providing a direct view of the dynamic forces and structures associated with AGN. These lines are without apparent distinction in AGNs of any kind [73, 86, 93] and have been of great help in supporting the unified model.

Observation of the coronal line region (CLR) show that this region is probably closer to the AGN than the NLR and, therefore, is associated with the outflow component [71]. Murayama & Tanigushi (1998a) [73], based in the [Fe VII] line, proposed that this region arises from the inner wall of the AGN's dusty torus, since Seyferts 1 show CLR emission excess with respect to Seyferts 2, considering the unified model [4] . This means that the radiation of the CLR is anisotropic, so a statistical study of its properties can be used to estimate the angle of vision to the

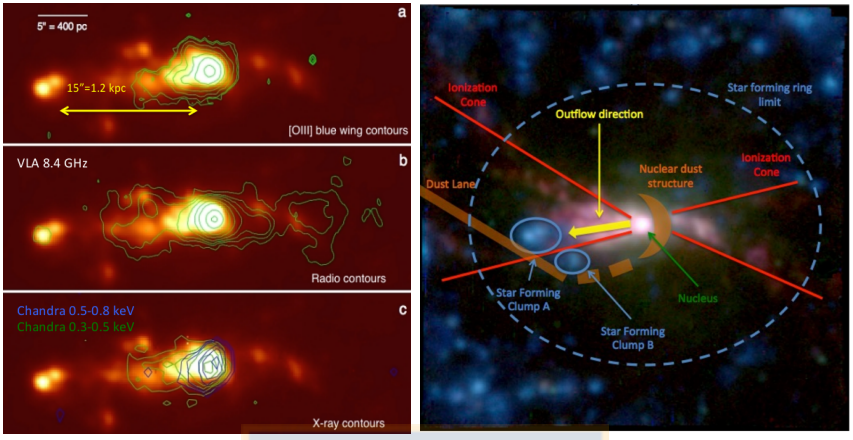

Figure 1.9: An outflow in NGC 5643 revealed by Muse. Left panel: Hα map (background) plus (a) [O III] emission line contours in the blue wing (v < -400 km s^{-1}), (b) 8.4 GHz radio contours from VLA observations, and (c) Chandra X-ray contours in the nuclear regions of NGC 5643. Right panel: Scheme denoting structures observed by MUSE in the nuclear regions of this galaxy, where two star forming clumps are shown, which are thought as possible signs of positive feedback by the authors. From Cresci et al. (2015) [21].

dust torus of several types of Seyfert galaxies and to better fit conical models for the AGN outflow.

Identifying low velocity outflows requires relatively high spectral resolutions and two-dimensional spectroscopy (integral-field spectrographs) in order to disentangle the different velocity components present: from the galactic disk, and from outflow(s) and/or inflow(s) [98, 106]. Moreover, in some special cases these outflows are detected more frequently as redshifted, rather than blueshifted, winds since the light from the ionized regions reaches us preferentially from the receding side of the outflow which, for the line-of-sight, is more illuminated by the AGN [e.g., 59], and the kinematics can often be modeled as a combination of a biconical outflow and a rotating disk coincident with the molecular gas [33, 72]. A better understanding of low velocity outflows in nearby Seyferts is important to understand the kinematics of Seyfert galaxies

at higher redshift, which could share the same model. An example of an outflow modeled with a biconical shape is presented in Figure 1.9, the data was obtained through the IFU MUSE on the VLT telescope, observing the nuclear regions of NGC 5643.

1.1.6 AGN Feedback

Outflows could be very important for the evolution of galaxies because they can be the most efficient way for the interaction between the AGN and its host galaxy, a process called AGN feedback, affecting the interstellar medium and the star formation. Several works explored whether this process triggers (positive feedback) or extinguishes (negative feedback) the host galaxy star formation [31, 47]. Empirical scaling relations between the masses of the SMBH and the host-galaxy bulge [e.g., 40], and between the AGN luminosity and the molecular outflow velocity [107] or dynamical mass [60], have motivated a more intensive study of this effect.

It can be shown that the growth of the SMBH by accretion in an AGN could have an important effect on its host galaxy: The binding energy of the galaxy bulge of mass M_{gal}, is $E_{gal} \approx M_{gal}\sigma^2$, where σ is the velocity dispersion in the galactic bulge. Considering that the mass of the black hole is related with the mass of the galactic bulge in the form: $M_{BH} \approx 1.4 \times 10^{-3} M_{gal}$ [41, 52], and assuming a mass-to-energy conversion efficiency for the accretion process of 10% [100], so that the energy released by the growth of the black hole is given by $E_{BH} = 0.1 M_{BH} c^2$. The binding energy of the black hole divided by that of the galaxy bulge is: $E_{BH}/E_{gal} \approx 1.4 \times 10^{-4}(c/\sigma)^2$. Since the majority of galaxies have $\sigma < 400$ km s^{-1}, the ratio E_{BH}/E_{gal} usually is > 80. Therefore, if a small fraction of this energy can be transfered to the gas, an AGN can have a profound effect on the evolution of its host galaxy.

According with Fabian (2012) [31], the feedback mechanisms can occur in two ways: one known as a "kinetic", "radio" or "maintenance" mode, well observed on X-rays, which generally operates in hot-halo galaxies or in the center of a cluster or group of galaxies, and another denominated as "radiative" or "quasar" mode, which operates, or operated, in a typical bulge when the accreting black hole is close the

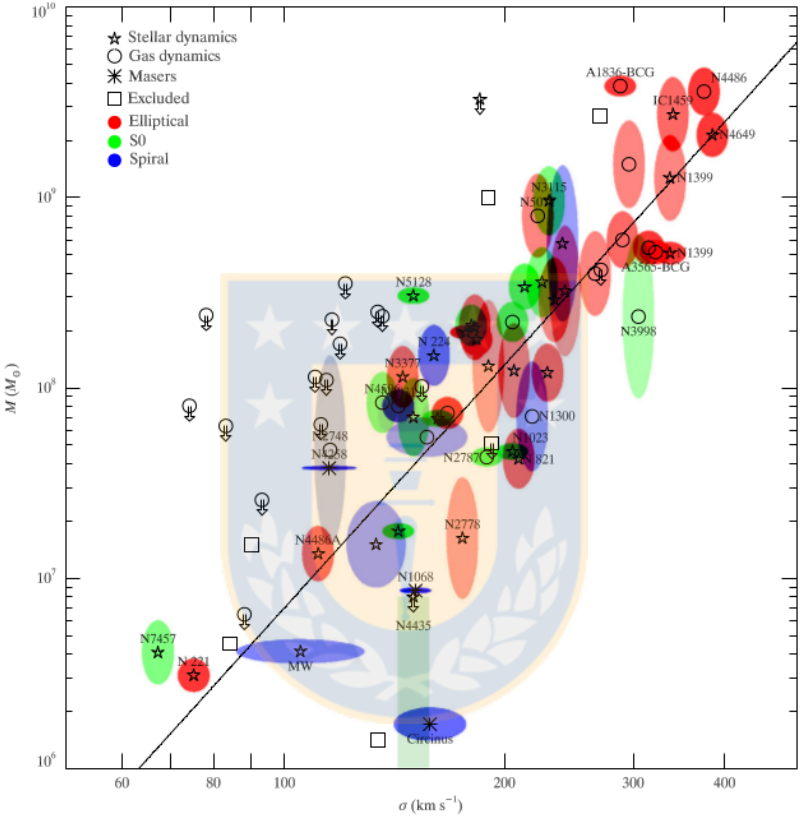

Figure 1.10: M-σ relation. The colors indicate different galaxy types and the symbols indicate the method of BH mass measurement. Arrows indicate the 3σ upper limits to BH mass. The line is the best fit relation to the full sample. This relation is obtained for galaxies with available dynamical measurements. From Gültekin et al. (2009) [40].

Eddington limit ($L_{edd} = 1.5 \times 10^{38}\ M_{BH}/M_\odot$ erg s^{-1}). It is most concerned with pushing cold gas.

Table 1.2: Different outflow properties compared with accretion parameters in the literature and this work. The rightmost column are the references: (1) Müller-Sánchez (2011) [72]; (2) Storchi-Bergmann (2010) [106]; (3) Davide Lena (2015) [59]; (4) Barbosa et al. (2009) [7]; (5) Riffel et al. (2011) [89]; (6) Riffel et al. (2013) [90] and (0) this work.

Galaxy	$\dot{M}_{out}$ ($M_\odot$ yr^{-1})	V_{out} (km s^{-1})	$\dot{M}_{acc}$ ($M_\odot$ yr^{-1})	$\dot{E}_{out}$ (10^{42} erg s^{-1})	L_{bol} (10^{42} erg s^{-1})	$\dot{E}_{out}/L_{bol}$	Ref
NGC 1068	9	1900 ± 80	0.015	5	88	0.05	1
NGC 2992	120	200 ± 20	0.015	2.5	85	0.029	1
NGC 3783	2.5	220 ± 20	0.003	0.07	180	0.0004	1
NGC 4151	2.4	600	0.013	0.24	73	0.0032	2
NGC 6814	7.5	120 ± 15	0.014	0.08	80	0.001	1
NGC 7469	4	130 ± 14	0.04	0.06	250	0.0002	1
NGC 1386	0.1	250	0.0003	0.0133	1.8	0.007	3
NGC 2273	31.2	160-400	0.00009	0.0044	1.014	0.0043	4
NGC 3227	15.8	180	0.00073	0.00068	8.24	0.000082	4
NGC 3516	51	265	0.0041	0.0048	45.98	0.000104	4
NGC 4051	1.2	120-170	0.00011	0.000034	1.3	0.0000261	4
Mrk 1066	0.06	500	0.003	0.00601	17	0.0003535	5
Mrk 79	3.5	75	0.035	0.034	200	0.00017	6
ESO 362-G18	0.15	394	0.013	0.0092	130	0.00007	0

The feedback process can be measured in form of the ratio between the kinetic power $\dot{E}_{out}$ of the outflow component with the accretion power - in form of the bolometric luminosity L_{bol}- of the AGN: $\dot{E}_{out}/L_{bol}$. There are different ways adopted to obtain the kinetic power, for example Lena (2015) [58] uses the equation $\frac{1}{2}\dot{M}_{acc}(V_{out}^2 + 3\sigma^2)$, while in Barbosa et al. (2009) [7], the formula used is $\frac{1}{2}\dot{M}_{acc}V_{out}^2$ and Müller-Sánchez et al. (2011) [72] use $\frac{1}{2}\dot{M}_{acc}(V_{out(maximum)}^2 + \sigma^2)$, where $\dot{M}_{acc}$, V_{out} and σ are the mass accretion rate, the adopted outflow velocity and the velocity dispersion. A summary of these quantities is shown in table 1.2., preserving the procedures used by their authors to obtain the $\dot{E}_{out}/L_{bol}$ ratio, except for Mrk 1066, where those were obtained from the outflowing component [Fe II] following the Lena's equation. As can be seen in this table, the kinetic power of the outflow represents only about few 10^{-3-5} of the available accretion power (0.1% to 0.001%). It is thought that about 0.5% L_{bol} is required to significantly affect the

evolution of the ISM in the host galaxy [46] so, in the sample of table 1.2, only NGC 1068 and NGC 1386 AGNs would actually do that.

1.2 This research

In this work, results obtained from integral field spectroscopy observations of the nuclear region of ESO 362-G18 (a.k.a. MCG 05-13-17), a nearby galaxy of morphological type Sa [MGT; 66] or S0/a [RC3; 24] [1] harbouring a Seyfert 1.5 nucleus [9] are present. ESO 362-G18 has a redshift of 0.012445 and a systemic velocity of 3731 km s^{-1} [82] or 3707 km s^{-1} [65]; the former estimate is considerer since it represents the data quite well. Assuming H_0=73.0 km s^{-1} Mpc^{-1}, this corresponds to a distance of 50.8 Mpc, and a linear scale of 246 pc $arcsec^{-1}$. Previous studies estimated a morphological position angle (PA) of 160° and a disk inclination (i), ranging from 37° to 54° [34, RC3, respectively]. ESO 362-G18 has been studied in the radio, NIR, optical, UV, and X-ray; its nucleus has typically been classified as Seyfert 1 [MGT, 1, 9, 34, 70, 92]. In Figure 1.11 an Structure map of this galaxy is shown, the magenta square denote the FOV of the observation used in this thesis.

Previous studies indicate that ESO 362-G18 is a highly disturbed galaxy [70] with a "long faint plume" to the NE [19]; this plume is likely an infalling less massive galaxy 10" to the NE, i.e. a minor merger. The emission-line maps of Mulchaey et al. (1996) [70] reveal strong [O III] emission centered near the continuum peak with a fan-shaped emission of ∼10" in the SE direction, roughly along the host galaxy major axis and coincident with the strongest Hα emission which is more symmetrically distributed about the nucleus. Mulchaey et al. (1996) [70] estimated that the highest excitation gas is located ∼7" southeast from the nucleus on one edge of the ionization cone, but Bennert et al. (2006) [9] found that only the central ±3" show line ratios typical of AGN ionized gas, and confirm the suggestion of Fraquelli et al. (2000) [34] that the ionization parameter is peaked in the nucleus and rapidly decreases within the narrow line region (NLR) based on the increased

[1] The resulting rotation curves or velocity maps in barred galaxies [22, 28] could be compared with that of ESO 362-G18 and thus rule out the presence of bars in this galaxy, confirming its S0/a morphology.

[OII]/[O III] ratio. Fraquelli et al. 2000 [34] also suggest that the nuclear continuum ionizes the gas in the disk along PA = 158°, giving rise to the fan-shaped region observed in [O III]. Arcsecond resolution *cm* radio maps of ESO 362-G18 do not show any obvious extensions [74]. Bennert et al. (2006) [9] find that the spectra out to r $\sim$ 11" northwest and out to r $\sim$ 6" southeast have line ratios which fall in the regime of [H II] regions. Indeed, Tsvetanov et al. (1995) [111] identify 38 [H II] regions in their ground based Hα+[N II] image of ESO 362-G18, distributed in a cloud around the nucleus with distances between 3-18".

The nuclear optical spectrum is dominated by broad permitted lines and narrow permitted and forbidden lines [92] and shows a featureless nuclear continuum due to the AGN [34], and main stellar features of Ca II K, G band, Mg I b and Na I D, as well as high order Balmer absorptions lines outside the nucleus. A broad Balmer decrement $H\alpha_{broad}/H\beta_{broad}$ of 5.7 indicates a slightly higher reddening of the broad line region (BLR) with respect to the central NLR [9].

NIR spectroscopy [87] shows strong, broad H I and He I lines, with an FWHM of $\approx$4500 km s^{-1} and $\approx$5400 km s^{-1}, respectively. Besides, numerous forbidden lines are seen, including high-ionization lines of [S IX], [Si X], and [Si VI]. The Brγ and H_2 molecular emission lines are observed as well, although they are intrinsically weak. The NIR continuum emission present stellar absorption features of Ca II , CO in H band, and the 2.3 μm CO band heads in K band on top of a steep power-law like the continuum.

The most recent detailed study of this galaxy has been realized by Agís-González et al. (2014) [1]. Their most important result was to detect a large variability in X-ray absorption which they explain as a clumpy, dusty torus lying in a compact region within $\sim 50 r_g$ (probably with 7 r_g, $1 r_g = GM_{BH}/c^2$) from the central black hole. They also estimated an inner accretion disk inclination of i=53° $\pm$ 5°, i.e. aligned with the large scale galaxy disk (RC3; 54°).

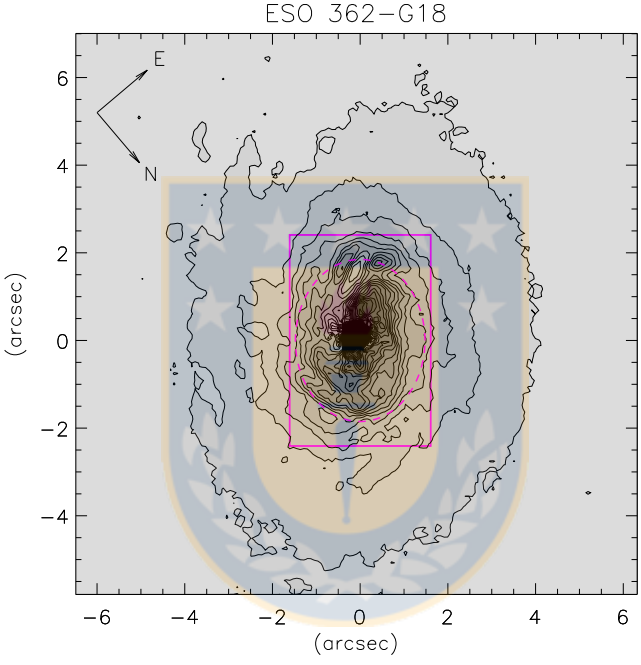

Figure 1.11: Structure map of ESO 362-G18, the magenta square indicate the field of view of the observation and the magenta ellipse denote a circumnuclear ring inclined with the adopted galaxy inclination. From this thesis.

Chapter 2

Observations and data Processing

The observations were obtained with the Integral Field Unit of the Gemini Multi-Object Spectrograph (GMOS-IFU [37]) at the Gemini South telescope on the night of December 23, 2014 (Gemini project GS-2014B-Q-20). The observations consisted of two adjacent IFU fields (covering 5×3.5 arcsec^2 each) with a spatial dithering of 0."5 resulting in a total angular coverage of 5×4 arcsec^2 around the nucleus. Two exposures of 900 seconds were obtained for each field, slightly shifted and dithered to correct for the detector defects after a combination of the frames. The seeing during the observation was 0."7, as measured from the FWHM of a spatial profile of the calibration standard star. This corresponds to a spatial resolution at the distance of the galaxy of 167 pc.

The selected wavelength range was 4092-7338 Å, in order to cover the Hβ λ4861, [O III]$\lambda\lambda$4959,5007, Hα+[N II] $\lambda\lambda$6548,6583 and [S II]$\lambda\lambda$6716, 6731 emission lines, observed with the grating GMOS B600-G5323 (set to central wavelength of either λ5700 Å or λ5750 Å) at a spectral resolution of R $\approx$ 1688 (with 0.50 Å per pixel) or a velocity dispersion (σ) of $\approx$ 75 km s^{-1}. Wavelength calibration is expected to be accurate to the order of 8 km s^{-1}.

The data reduction was performed using specific tasks developed for GMOS data in the GEMINI.GMOS Version 1.13 package, as well as

generic tasks in IRAF[1]. The reduction process [see 57] comprised bias subtraction, flat-fielding, trimming, wavelength calibration, sky subtraction, relative flux calibration, building of the data cubes at a sampling of 0."08×0."08, and finally the alignment and combination of the 4 data cubes. The resulting cube contains 2100 spectra after deleting bad spaxels, corresponding to a spatial coverage of 60 × 35 spaxels (4.8 × 2.8 arcsec^2), with each spectrum containing 6399 spectral pixels.

In order to measure the stellar kinematics and create an emission-line-only cube, the Penalized Pixel Fitting technique (pPXF) [16] was employed using The MILES Stellar Library [95] as stellar templates, which consists of spectra for $\sim$ 1000 stars obtained mainly with the 2.5m INT telescope. These spectra have been achieved at a spectral resolution of 2.51 Å (FWHM) or $\sigma \sim 64$ km s^{-1} and cover a spectral range of 3525Å to 7500Å. As the spectral resolution is different from the data (75 km s^{-1}), the spectral resolution of the templates was degraded to the GMOS resolution. To ensure the reliability of the stellar kinematic measurements, the data cube was spatially binned using the Voronoi binning method [see 15], creating bins with a minimum signal-to-noise (S/N) ratio of 25. Spatial averages (over large and small apertures) of spectra over different regions of the cube were first used to identify the 20 template spectra most used in the fits. These twenty spectra were then used to fit all individual bins in the cube. Before running pPXF, the BLR emission from the AGN was masked, present mainly within the inner seeing disc of 0."68 (167 pc). The resulting best fit templates were also used to create an "emission-line-only" spectrum for each spaxel. Examples of this process are shown in Fig. 3.2.

The centroid velocities, velocity dispersions and the emission-line fluxes of the gas were initially obtained from the emission-line-only cube by fitting a single Gaussian to the Hα, Hβ, [N II], [O I], [O III], [S II]λ6716 and [S II]λ6731 emission lines using FLUXER[2], which allows us to determine the residual continuum level around the emission lines in an

[1]IRAF, is distributed by the National Optical Astronomy Observatories, which are operated by de Association of Universities for Research in Astronomy, Inc., under cooperative agreement with the National Science Foundation.

[2]Interactive IDL routine written by Christof Iserlohe. http://www.ciserlohe.de/fluxer/fluxer.html

interactive way (this is necessary for the [S II] lines since they are very close to the broad component of Hα). The resulting gaseous velocities are similar to those obtained from the Gas AND Absorption Line Fitting code [GANDALF; 96] and PROFIT [88]. To obtain the final velocity and dispersion maps, a sigma clip of 3σ was performed for all radial and velocity dispersion maps except in the nuclear regions of [O III] (because of their high S/N ratio).

The kinematic position angles (hereafter PA) for both stars and gas were estimated using Kinemetry: a generalisation of photometry to the higher moments of the line-of-sight velocity distribution [53]. The systemic velocity (hereafter V_{sys}) of 3731 km s^{-1} was taken from Paturel et al. (2003) [82].

A double-Gaussian fit to the [O III] and Hα emission lines was performed using a series of Python codes. To decide whether the observed line profile is better fit with a single or double Gaussian, the Akaike Information Criterion [3] was used with the additional caveats that all Gaussian amplitudes are positive.

Chapter 3

Results

The upper left panel of Fig. 3.1 presents the Gemini acquisition image filter r of ESO 362-G18, where the posited minor merger approaching from the NE direction is also clearly seen; the rectangle shows the field-of-view (hereafter FOV) of the IFU. The upper right panel shows the stellar continuum image obtained from the IFU datacube by integrating the flux within a spectral window from λ 5345 Å to λ 5455 Å. It is assumed that the nuclear position coincides with the location of the continuum peak in this image.

In the lower panel, four spectra from the locations marked as 1 (Nucleus), 2 and 3 (intermediate regions) and 4 (boundary region) are present in the IFU image and extracted within apertures of 0".2 × 0".2. The nuclear spectrum (identified as 1 in Fig. 3.1) shows broad Hα and Hβ components, which has led to the classification of ESO 362-G18 as a Seyfert 1 galaxy [34], and also narrow [O III] $\lambda\lambda$ 4959,5007 Å, [O I] $\lambda\lambda$ 6300,6363 Å, [N II] $\lambda\lambda$ 6548,6583 Å and [S II] $\lambda\lambda$ 6717,6731 Å emission lines. Variations in the broad component of the Hβ emission line, very common in this type of objects, have led to this galaxy being occasionaly classified as a Seyfert 1.5.

I created a "structure map" of ESO 362-G18 (right panel of Fig. 3.5) by running the IDL routine "unsharp mask" on an image obtained with WFPC2 (Wide Field Planetary Camera 2) through the filter F547M aboard the Hubble Space Telescope (hereafter HST). Inspection of the dust structure shows signs of spiral arms together with

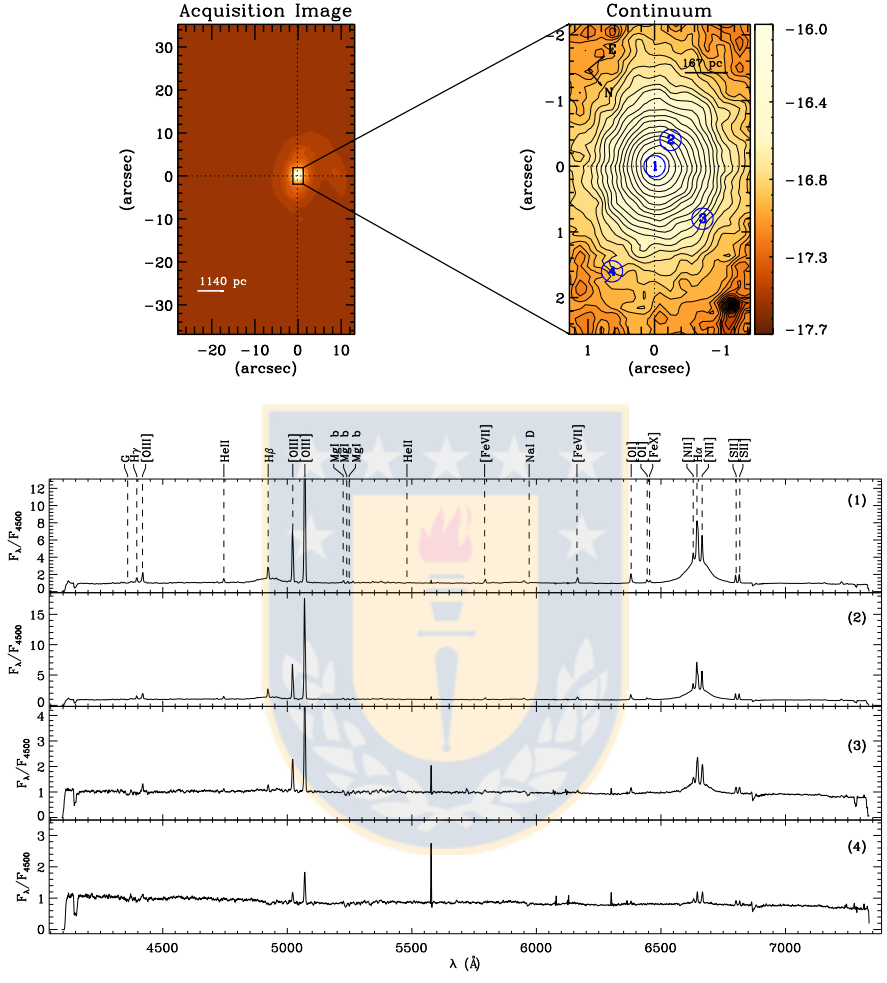

Figure 3.1: Acquisition and continuum image of ESO 362-G18 plus some spectra. Top left: acquisition Gemini GMOS image, the rectangle shows the field of view of the IFU observation. Top right: continuum image of ESO 362-G18 (see Chapter 3). Bottom: spectra corresponding to the regions marked as 1, 2, 3 and 4 in the IFU image. From this work.

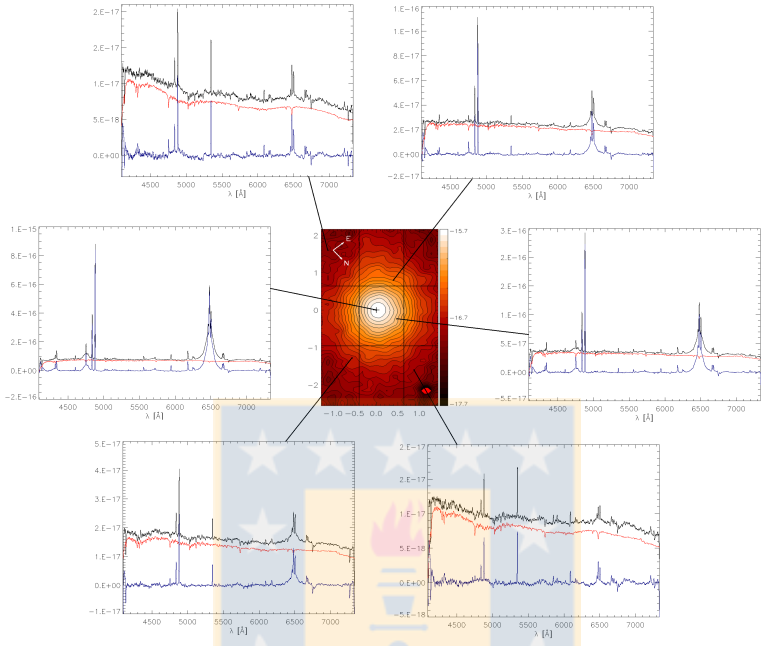

Figure 3.2: Best continuum fitting with Ppxf. Fits of the Gemini GMOS spectra of ESO 362-G18 using the MILES Stellar Library [95] for six spaxels. The spectra (black lines) and their corresponding fits (red lines) at different locations in the Gemini GMOS field are shown, the individual spatial locations being indicated by lines on the continuum image of ESO 362-G18 (the same as Fig. 3.1 upper right panel). The vertical and horizontal lines in this continuum image delimit the small apertures where spatial averages of spectra were taken to obtain the spectra most used by pPXF (whose contributions were more important to do the best-fit to the continuum). The vertical position of the best-fitting spectra obtained with pPXF [16] are slighly shifted for legibility, the residual (emission line only) spectra being presented on the bottom (blue lines). Axes of the continuum image are in arcseconds. Vertical axes of spectra panels are in erg cm^2 s^{-1}. From this work.

stronger obscuration to the Southwest than to the Northeast. Then it is concluded that the SW is the near side of the galaxy. This is also consistent with flux asymmetries (Section 3.1) and a trailing spiral pattern (Section 3.2).

3.1 Morphology and excitation of the emitting gas

In Fig 3.3 the flux distributions derived from single Gaussian fits in the Hα, Hβ, [N II]λ6583 Å, [O I]λ6300 Å, [O III]λ5007 Å and [S II]λ6716 Å emission lines are presented. The flux distributions show a relatively smooth and symmetric pattern for all the emission lines, slightly elongated along the kinematic major axis (see Figures 3.6 and 3.7), as expected given the inclination. The highest fluxes are within the inner 1" (246 pc). If the best fitting two-dimensional Gaussian is subtracted from these flux distributions, the greatest asymmetries are found in the southwest, implying a stronger presence of dust here. This supports my previous interpretation of the SW as the near side of the galaxy.

Maps of the estimated electron density and the [N II]/Hα, [O I]/Hα, Hα/Hβ, [O III]/Hβ line ratios are presented in Fig. 3.4. The electron density was obtained from the [S II]$\lambda\lambda$6716/6731 Å line ratio assuming an electronic temperature of 10000 K [80]. The electron density reaches a peak value of $\sim$ 2900 cm^{-3} at the nucleus, decreasing to 1000 cm^{-3} at 1" and 800 cm^{-3} at 1.5" from the nucleus. These values are in agreement with those obtained by Bennert et al. (2006) [9] who estimated values from 1000 cm^{-3} up to 2500 cm^{-3} in that region.

The [N II]/Hα line ratio shows values of 0.55-0.78 within the inner 1", and reach its highest values - close to 0.9 - in a nuclear-centered ring of radius 1.5". The [O III]/Hβ ratio varies between 5.6 and 9 in the inner 0.5", with a depression in the nucleus and increasing to 11 at 1". Taking into account both the line ratios, the values can be considered typical of Seyfert galaxies [17].

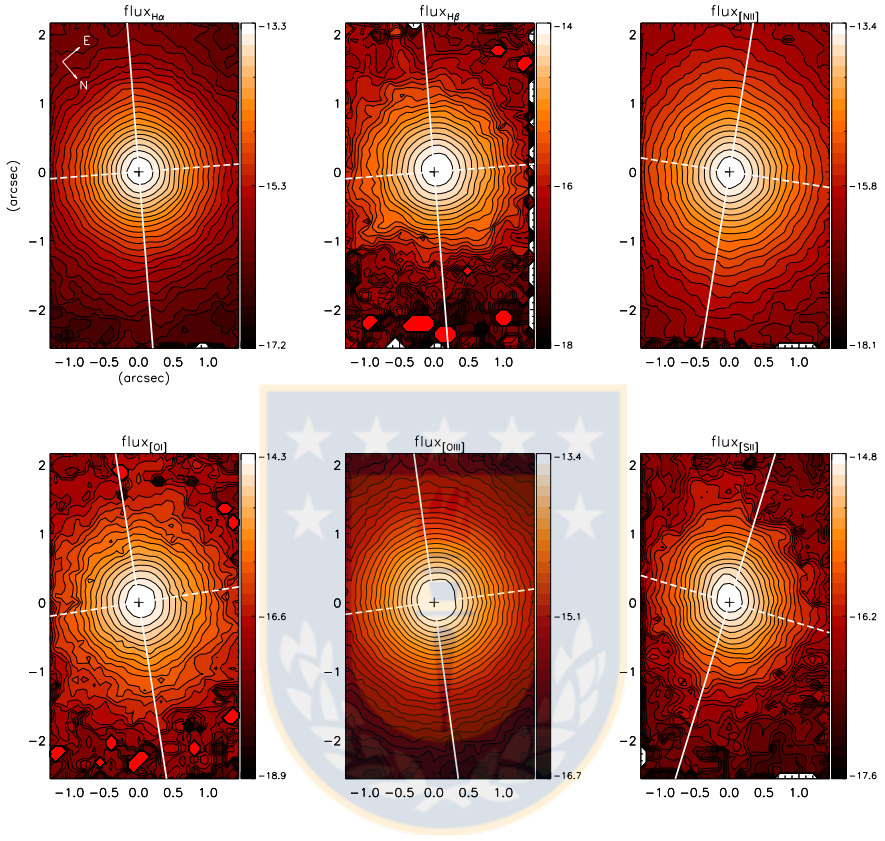

Figure 3.3: Integrated fluxes: maps of the Hα, Hβ, [N II], [O I], [O III] and [S II] integrated fluxes in logarithmic scale (erg cm^2 s^{-1} per pixel) following the color bar to the right of each panel. Axes are in arseconds with respect to the nuclear continuum peak. Crosses mark the continuum peak and the solid (dashed) lines mark the major (minor) axis of the kinematics of the respective line. The panels follow the color bar shown on the right side each. From this work.

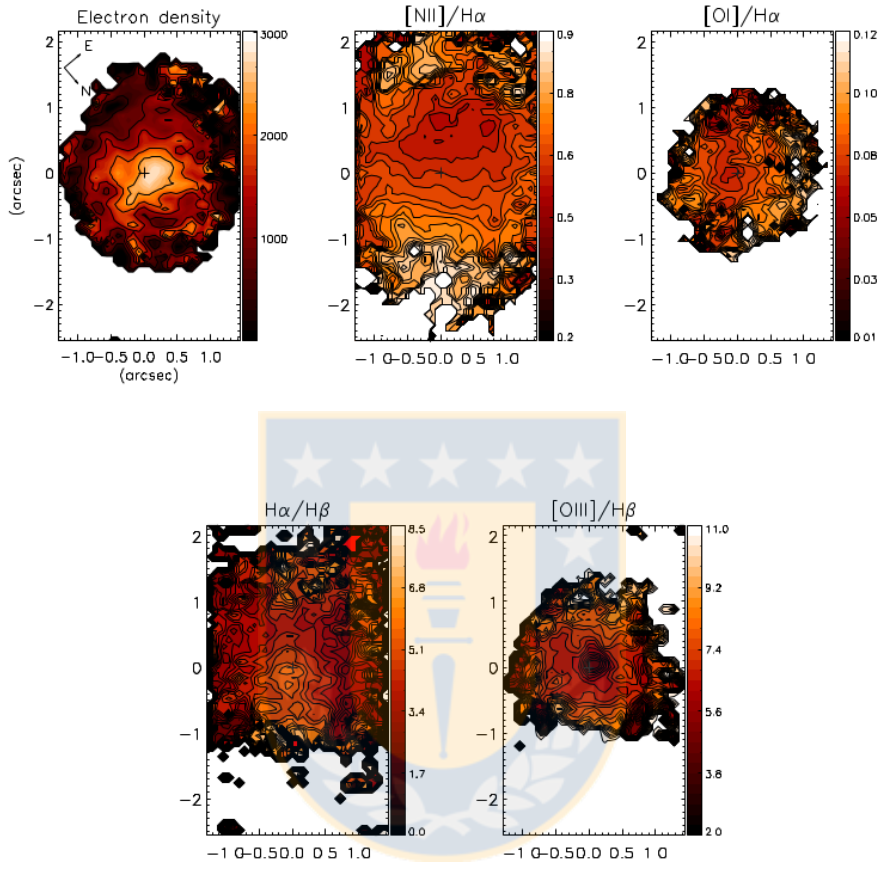

Figure 3.4: Maps of the estimated electron density (cm^{-3}) distribution and important emission line ratios: [N II]/Hα, [O I]/Hα, Hα/Hβ and [O III]/Hβ. The cross represent the continuum peak. The panels follow the color bar shown on the right side each. From this work.

3.2 Stellar kinematics

The stellar velocity ($V_\star$) field, obtained from pPXF, is shown in the left panel of Fig. 3.5. It displays a rotation pattern reaching amplitudes of ≈ 75 km s^{-1} within the field of view, with the line of nodes oriented ap-

proximately along the Northwest–Southeast direction, with the SE side approaching and the NW side receding. With the adopted orientation, this implies trailing spiral arms as expected. The stellar velocity dispersion (Fig. 3.5.) reaches values of 105 km s^{-1} at the nucleus, staying up to 80 km s^{-1} to the NW and decreasing to 50 km s^{-1} to the SE and toward the edges of the FOV.

The code Kinemetry [53] is used to obtain the position angles of the stellar kinematics at different radii from the nucleus. The resulting values range from 130° to 139°, then, the median value of 137° is chosen as the global kinematic position angle, as suggested by Krajnović et al (2006) [53, Appendix C]. This value is consistent with morphological major axes from the literature: between 110° and 160° (values taken from NED).

Assuming circular orbits in a plane and a spherical potential, the observed radial velocity at a position (R, ψ) in the plane of the sky is given by [10]:

$$V = V_s + \frac{ARcos(\psi - \psi_0)}{[R^2[sin^2(\psi - \psi_0) + cos^2\theta cos^2(\psi - \psi_0)] + c^2 cos^2\theta]^{p/2}}$$

where θ is the inclination of the disk (with $\theta = 0$ for a face-on disk), ψ_0 is the position angle of the line of nodes measured with respect to the x-axis within the field shown; V_s is the systemic velocity, R is the radius and A, c, and p are parameters of the model. The kinematical centre is assumed to be cospatial with the peak of the continuum emission, the inclination of the disk was fixed to 37°, obtained from the apparent axial ratio [34, 115] under the assumption of a thin disk geometry, and the V_{sys} was fixed to 3731 km s^{-1} [82].

I used Levenberg-Marquardt least-squares algorithm to fit the rotation model to the velocity map. The resulting parameters A, c and p, are 203 km s^{-1}, 1".09 and 1.93, respectively.

The V_{sys} corrected to the heliocentric reference frame was about the same as the one initially taken so that velocity (3731 km s^{-1}) is used as the systemic velocity.

The model stellar velocity field and velocity residuals are shown in Fig. 3.5.

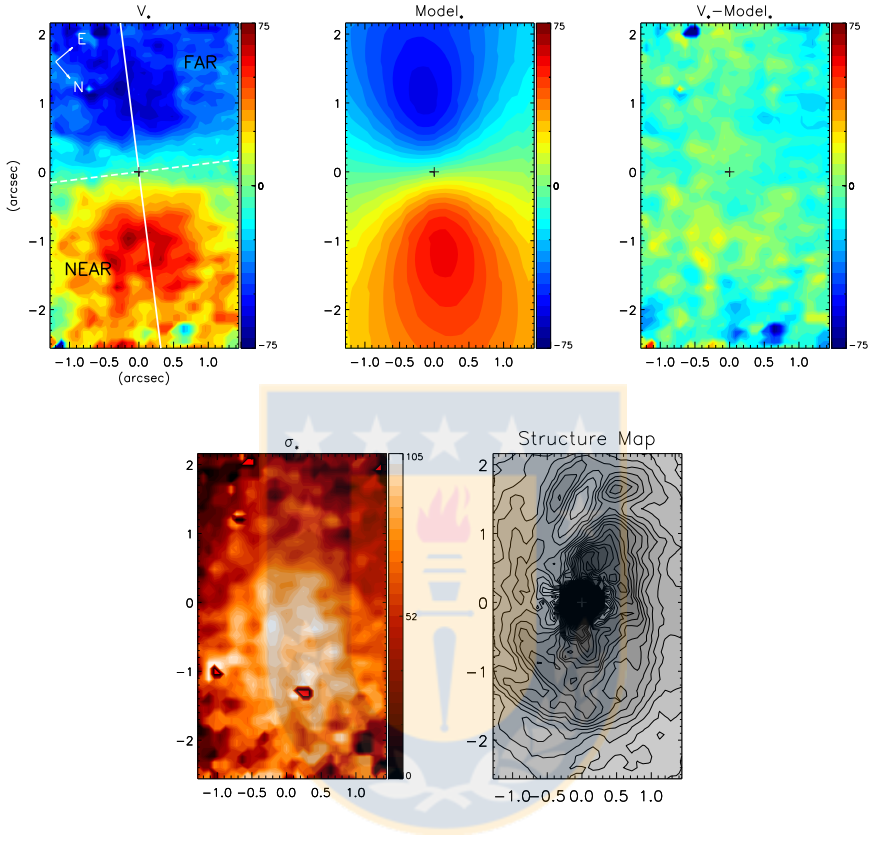

Figure 3.5: Stellar kinematics and rotation model plus structure map. The observed stellar velocity field (km s^{-1}), stellar rotation model, residual velocity field (observed - model), stellar velocity dispersion (km s^{-1}), and the structure map of ESO 362-G18 are shown. The solid white line marks the position of the kinematic major axis and the dashed white lines that of the minor axis. The cross represent the continuum peak. The panels follow the color bar shown on the right side each (except in the Structure map). From this work.

3.3 Gas kinematics

In the left column of Fig. 3.6 and first and third panels of Fig. 3.7, the centroid velocity maps -from a single Gaussian fit- of the [N II]λ6583 Å, Hα and [O III]λ5007 Å emission lines are shown.

All velocity maps predominantly show characteristic patterns of a rotating disk with amplitudes ranging from 66 km s^{-1} up to 82 km s^{-1}. Fitting these velocity fields with Kinemetry [53], global kinematic position angles (PAs) are obtained, ranging between 121° and 139° [53, Appendix C]. For Hα, the global PA is fixed as the mean value between the global PAs of this line (139°) and that of Hβ (130°), since the PA in Hα varies widely at different radii, given no credible values at times.

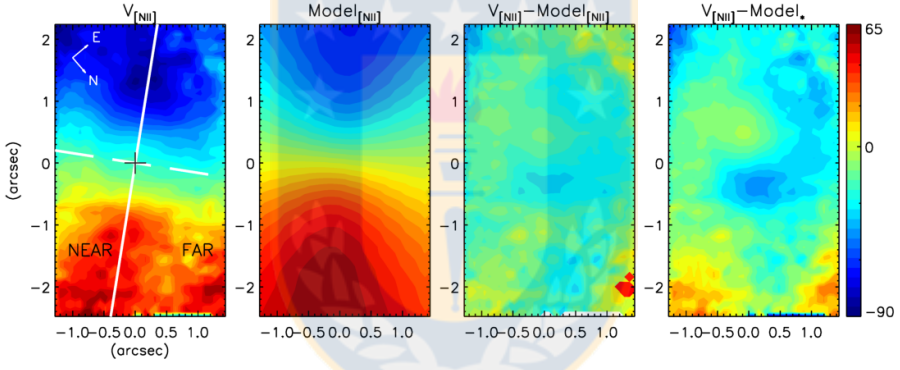

Figure 3.6: N II kinematics, rotation model and different residuals. Specifically: the observed [N II] velocity field (km s^{-1}), [N II] rotation model, residual velocity field (observed - [N II] model), and residual velocity field (observed - stellar model). The solid white line marks the position of the kinematic major axis and the dashed white lines that of the minor axis. The cross represent the continuum peak. The panels follow the color bar shown on the right side of the residual (observed - stellar model) panel. From this work.

For each given emission line, the radial variations of the PA does not exceed 20°, and all emission line PAs are in rough agreement (within 16°) with the stellar kinematic PA, except for [S II] where the difference is 24°.

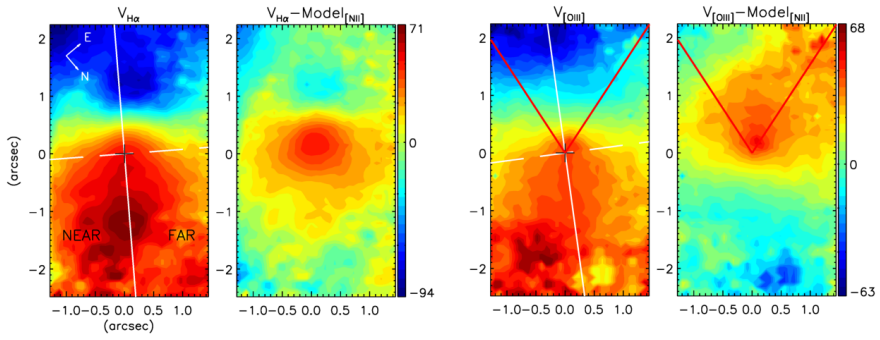

Figure 3.7: Some gaseous velocity maps and residuals: the emission line gas velocity fields and residual velocity fields (observed - [N II] model) for Hα and [O III]. The panels first and third show the gaseous centroid velocities (km s^{-1}) obtained from a single Gaussian fit. Here the cross marks the location of the stellar continuum peak, and the solid and dashed lines delineate the major and minor kinematic axes as derived using Kinemetry (Section 3.3). For the [O III] velocity map (and residual velocity field) the red lines mark the bounds of the ionization cone (I use an opening angle of 70° in agreement with the value ($\geq$60°) proposed by Fraquelli et al. (2000) [34]). The panels follow the color bar shown on the right side of the corresponding residual panel. From this work.

Inspecting the velocity maps of these emission lines, an offset of $\approx$ 0".5 (128pc) between the continuum peak and kinematic center the gaseous kinematics is observed for Hα, Hβ, [O I], and [O III], while no significant offset is present in [N II]λ6583 or [S II]λ6716. To more clearly visualize these offsets, the rotation curves of the stars and the stronger emission lines along their respective kinematic PAs are plotted in Fig. 3.8. The offsets cause an apparent asymmetry in the velocity fields within the FOV, reaching greater blueshifts than redshifts in the majority of cases. However, comparing this feature with previous long-slit spectroscopy of the inner 10" and 30" [9, 34, respectively], it can be inferred that this asymmetry is exclusively due to the offset in the kinematic center.

Since the [N II] emission line is both strong and without a significant

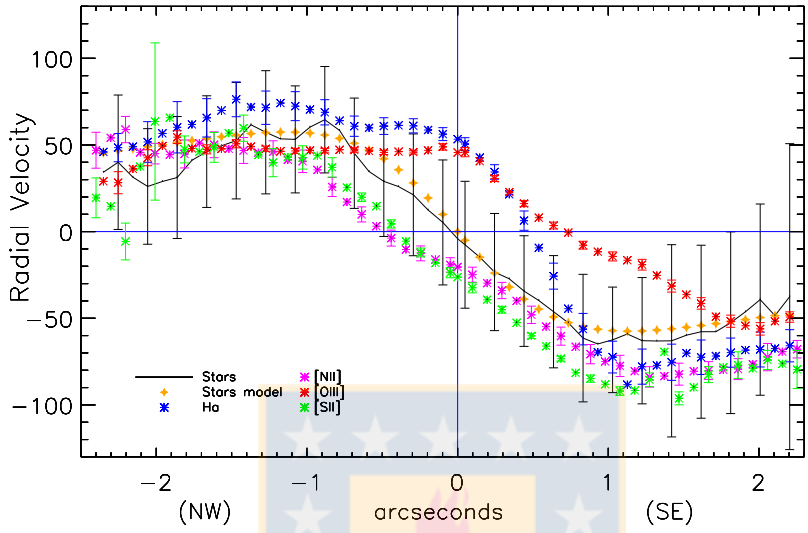

Figure 3.8: Radial velocity ("rotation curves") curves of the emission lines along with the Bertola model (Stars model) for the stellar kinematics, following the legend in the bottom left. The PAs along which these velocities were taken are those derived by Kinemetry (Section 3.3) for each emission line: 135° for Hα, 121° for [N II], 137° for [O III] and 113° for [S II]. The zero velocity (horizontal line) corresponds to a (heliocentric) velocity recession of 3731 km s^{-1}. Error bars in the corresponding color indicate the velocity errors determined by pPXF (stars) or Fluxer (Gaussian fitting to emission lines). The vertical line marks the position of the continuum peak. From this work.

kinematic offset from the stellar continuum peak, a "gas-kinematic" Bertola model is fitted to its velocity field, following the procedure outlined in Section 3.2. Once more the disk inclination is fixed to 37°, and the V_{sys} is fixed to 3731 km s^{-1}, and the kinematic center is assumed cospatial with the stellar continuum peak. The resulting values are 125 km s^{-1}, 1".06, 1.04 and 125° for A, c, p and the PA, respectively. This gas-kinematics model is shown in the second column of Fig. 3.6. The third and fourth columns of Fig. 3.6 show the residual velocity fields of

the emission line gas after subtraction of gas-kinematics model and the stellar velocity model, respectively. For all lines except [N II] and [S II] the above mentioned excess redshift is seen SE of the nucleus.

Maps of the velocity dispersion (henceforth referred to as σ before the name of the corresponding emission line) of the corresponding emission lines -deriving with a single Gaussian fit- are shown in Fig. 3.9. The uncertainty here is $\sim$75 km s^{-1}. The highest nuclear dispersions, $\gtrsim$200 km s^{-1}, are seen in $\sigma_{H\alpha}$ and $\sigma_{[N\,II]}$; leaving the nucleus, their dispersions decrease faster along the kinematic major axis than along the kinematic minor axis. On the other hand, $\sigma_{[O\,III]}$ is predominantly homogeneous in the non-nuclear regions with its nuclear value rapidly increasing to 150 km s^{-1}. In the next sections, this large nuclear dispersion is interpreted as due to the presence of a new offset velocity component which is most prominent in the nuclear region, causing blended profiles and thus non-reliable fits to a single Gaussian. The dispersion of the Hβ line is similar to that of Hα, while both $\sigma_{[O\,I]}$ and $\sigma_{[S\,II]}$ do not present centrally peaked distributions.

3.4 Position–velocity diagrams

To better constrain the emission-line kinematics, position-velocity (PV) diagrams (Fig. 3.10) have been constructed for the three strongest emission lines, [O III], Hα, and [N II]. These PV diagrams were made centered on the continuum peak and along PA 130° since this is the kinematic major axis found in the single Gaussian fit. The pseudo slit is 0.8" wide. The velocity prediction from the single Gaussian fit is superposed for an easy direct comparison.

While the PV diagram of [N II] shows a good agreement with the single Gaussian fit, the diagrams of both [O III] and Hα show a second velocity component redshifted by $\sim$150 km s^{-1} in the nuclear region. If the prominent emission in Hα and [O III] is seen from a larger velocity range, it may be noted that the most of the emission occurs at velocities below $\pm$ 500 km s^{-1} for both these lines.

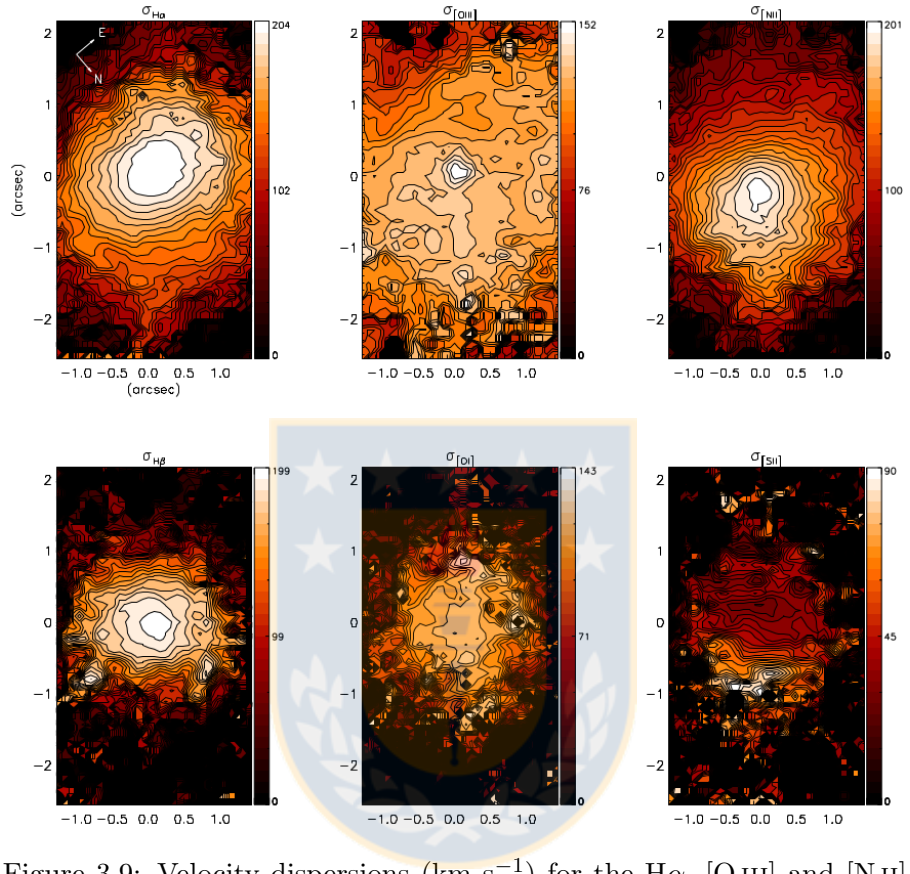

Figure 3.9: Velocity dispersions (km s^{-1}) for the Hα, [O III] and [N II] (up) and Hβ, [O I] and [S II] (down) emission lines. Each color bar is centered on the average velocity dispersion of the respective line. From this work.

3.5 Double Gaussian fit

Given the clear evidence for a second velocity component in some of the emission lines, the [O III] and Hα emission lines are fitted with double Gaussian profiles; these two lines were chosen as they have the highest signal-to-noise ratio among the double peaked lines. Given the clear velocity separation seen between the two components in the PV diagrams,

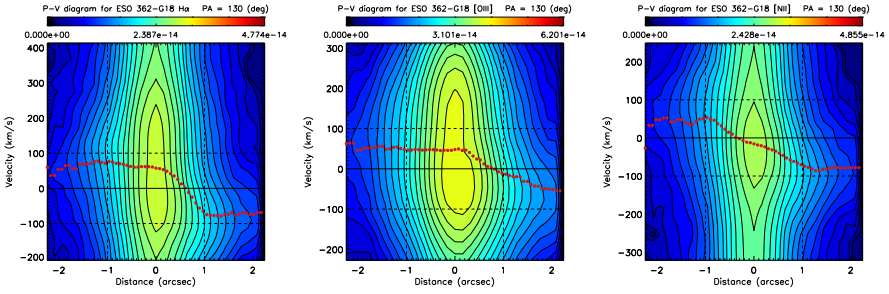

Figure 3.10: Position-velocity diagrams and velocity maps. From left to right: Position-velocity diagrams of Hα, [O III] and [N II] emission lines oriented at PA = 310°, which is along the kinematic major axis (and the ionization cone). Note that the spectra are continuum subtracted. Colors and contours denote flux following the color bar above each panel. The corresponding rotation curves obtained from the single Gaussian fit (see Section 3.3) are superimposed in red circles. The black solid line marks the zero velocity (V_{sys} = 3731 km s^{-1}), the dashed horizontal lines marks velocities of ± 100 km s^{-1}, and the dashed vertical lines marks offsets of ± 1" from the nucleus. The color bar above each panel indicates the integrated flux. Contours are in powers of $\sqrt{2}$, to trace both the faint and strong emission structure. From this work.

these components are discriminated by their radial velocity (rather than, e.g., width) and henceforth refer to them as the low-velocity component and the high-velocity component. The double Gaussian fit is made using a series of Python codes, mainly within the lmfit package[1], to fit the line profiles at each spaxel in the data cube and then extract radial and dispersion velocities, among other parameters. To decide whether the observed line profile is a better fit with a single or double Gaussian, the corrected Akaike Information Criterion (AIC_c) [3] is used with the additional caveats that all Gaussian amplitudes are positive. For the Hα emission line, the double Gaussian fit was performed after subtraction of the broad component (Fig. 3,1), which can be detected as far as ∼1" from the nucleus, even though the seeing was ∼0."7. This broad com-

[1]https://lmfit.github.io/lmfit-py/intro.html

ponent is also present in Hβ (Fig. 3.1). The AIC is useful to measure the relative quality between different statistical models. In this case it allows us to measure the accuracy of a fit made with 1 Gaussian and compare it with a fit of two Gaussian in a certain emission line.

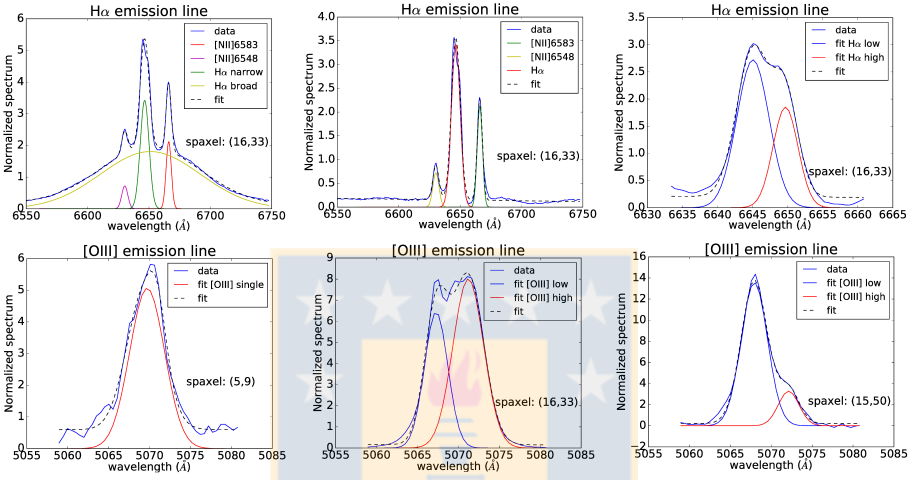

Figure 3.11: Double Gaussian Fitting. Upper panels: example multiple Gaussian fits to the Hα+[N II] $\lambda\lambda$6548,6583 Å emission lines. Bottom panels: Double or single Gaussian fits to the [O III] λ5007 Å emission line. Emission line profiles are normalized (see Section 3.5). In the top panels the fitting process used for the Hα+[N II] $\lambda\lambda$6548,6583 Å in a single nuclear spaxel is shown; from left to right: (1) the multiple Gaussian fit to Hα (one broad and one narrow component) and [N II] $\lambda\lambda$6548,6583 (one narrow component each) emission lines, (2) the same as (1) but with the broad Hα component subtracted out, and (3) the subsequent double Gaussian fit to the Hα line. In the bottom panels, examples of Gaussian fitting in the [O III] emission line in three different spaxels are present: the AIC_c is used to decide whether a single or double Gaussian fit is used. In spaxel 5,9 (to the NW) a single Gaussian provides a better fit, while in the spaxels near the nucleus (16,33) and to the SE (15,50) double Gaussians are required. From this work.

In the upper three panels of Fig. 3.11, a detailed example of the

fitting process to the Hα emission line in a nuclear spaxel is shown. These panels show the multi-component Gaussian fit to the Hα and [N II] $\lambda\lambda$6548,6583 emission lines, before (left) and after (middle) the subtraction of the broad Hα component, and the subsequent double Gaussian fit to the narrow Hα emission. In the bottom panels of the same figure, examples of single/double Gaussian fits are present for [O III] (as decided by AIC$_c$) in different spaxels ((x,y) axes) of the data cube.

The results of the two-component fits to [O III] and Hα are shown in Fig. 3.12. The left four panels show the velocity fields of the two components of Hα and [O III], and the two rightmost panels of Fig. 3.12 show the same major axis PV diagrams as Fig. 3.10 (along PA 130°), but this time overlapping the velocities of each of the two velocity components (high-velocity component in red and low velocity component in blue) along with the velocities obtained from the single Gaussian fit to the respective line (green), the velocities obtained by a single Gaussian fit to the [N II] line (brown) and the Bertola model fit to the stellar kinematics (black). According to AIC$_c$, the two-component fit is required only to the SE. To the NW, a single component fit gives better results. The lower [O III] velocity component has velocities ranging from -30 km s^{-1} to -135 km s^{-1} and a kinematic PA of $\sim$ 123°, while the higher [O III] velocity component shows values $\approx$ 200 km s^{-1} higher. The lower Hα velocity component shows velocities of -80 km s^{-1} to 70 km s^{-1}, with a PA of $\sim$ 123°, while the higher Hα velocity component show values of 100 km s^{-1} up to 255 km s^{-1}. The corresponding velocity dispersions are shown in Fig. 3.13. The low-velocity component of Hα shows a centrally peaked velocity dispersion map, while in the higher velocity component shows high dispersions only in disjoint regions $\gtrsim$0".6 from the nucleus. The low-velocity component of [O III] has systematically higher dispersions (except in the nucleus) in comparison to the high-velocity component.

3.6 The black hole mass

Black hole mass estimations for ESO 362-G18 were rigorously explored by Agís-González et al. (2014) [1]; the new observations allow us a better constraint on the value of the FWHM of $H\beta$ since a better spectral

resolution and two-dimensional data for this line is now available. The $H\beta$ profile is fitted with a double Gaussian using the lmfit package as described in Sec. 3.5, and use the FWHM of the broad component (hereafter FWHM$_{H\beta}$) to estimate the black hole mass.

Assuming a disc-like BLR geometry to avoid assuming a virial coefficient f, which can vary widely, Agís-González et al. (2014) [1] used the following expression:

$$M_{BH} = R_{BLR} FWHM^2 (4Gsin^2 i)^{-1}$$

where i is the angle between the line-of-sight (LOS) and the angular momentum vector of the disc-like BLR (53° ± 5°), R$_{BLR}$ is the radius of the BLR ($\sim$ 5.2 $\times$ 10^{16} cm), and G is the gravitational constant. Using the new value of FWHM$_{H\beta}$, 5689^{+398}_{-722} km s^{-1}, calculated in the inner 0".34 around the continuum peak (i.e., within the seeing), a black hole mass M_{BH} of $4.97^{+1.60}_{-1.61}$ $\times$ 10^7 M$_\odot$ is obtained, consistent with the value (4.5 ± 1.5 $\times$ 10^7 M$_\odot$) obtained by Agís-González et al. (2014) [1] and in a range typical of both narrow-line and broad-line Seyfert 1 galaxies [38, Fig. 4].

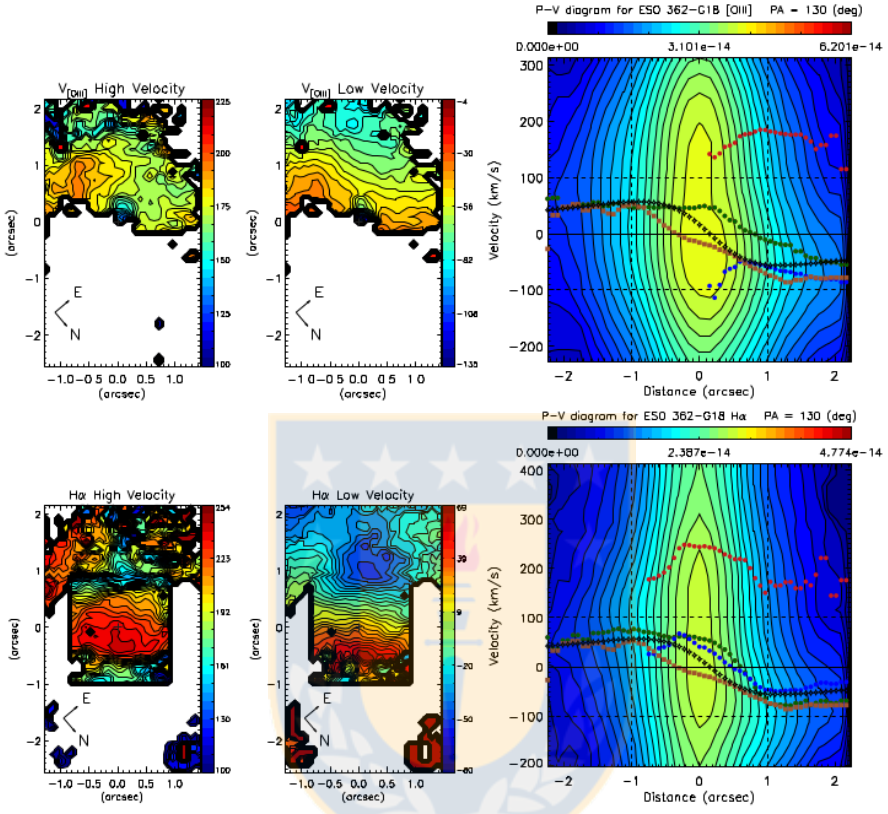

Figure 3.12: Position Velocity diagrams and Velocity fields in some emission lines of ESO 362-G18. From top to bottom these panels corresponding to [O III] and Hα, respectively. From left to right: Velocity fields of high-velocity and low-velocity components, while on the rightmost panels are present PV diagrams where the velocities of each component have been superimposed: blue and red points correspond to the low and high velocity components, respectively, while velocities obtained with a single Gaussian fitting are in green. For comparison, also in these PV diagrams, the [N II] velocity curve along the kinematic major axis (filled brown squares) and the derived model for the stars [open black stars; 10] is overplotted. In the PV diagrams, the black solid line marks the velocity, corrected by a $V_{sys} = 3731$ km s^{-1}, dashed horizontal lines mark $\pm$ 100 km s^{-1} velocities and dashed vertical lines marks $\pm$ 1" from the nucleus. The PV diagram contours are plotted as a power of $\sqrt{2}$, to reveal the faint as well as the strong emission structure. The color bar of the velocity fields show the velocities and represent the fluxes in the PV diagrams.

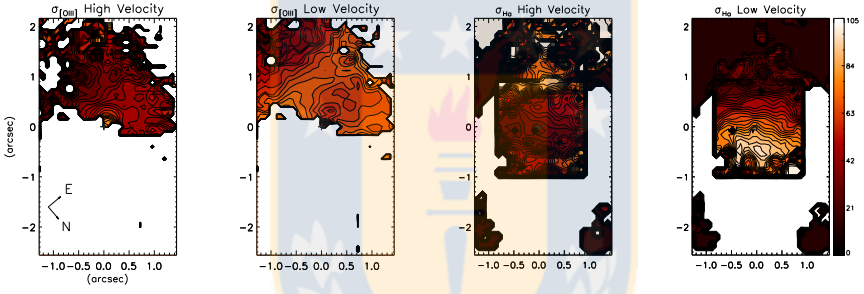

Figure 3.13: Dispersions of different emission line components. From left to right: the velocity dispersion of the [O III] and Hα high velocity and low-velocity components, respectively. The panels follow the color bar shown on the rightmost side. From this work.

Chapter 4

Discussion and Conclusions

The structure map (rightmost panel of Fig. 5) shows spiral arms which get increasingly fainter as they approach the nucleus. Given the scale of the FOV and asymmetries found after subtracting 2D-Gaussians from the flux maps of each emission line, the unusual spiral arm structure can be interpreted as a result of instabilities produced by the inner Lindblad resonance, which is expected to lie in the inner 1.6 kpc [54]. Thus, the unusually high value of the parameter p (>1.5) in the Bertola stellar model can be argued as a direct consequence of this resonance. The abundant dust seen in the structure map also supports the hypothesis of [102], that the presence of dust is a necessary condition for accretion onto the nuclear SMBH.

Previous studies of ESO 362-G18 have found an asymmetric [O III] image with a fan-shaped structure extending 10" from the nucleus to the SE, and a green continuum image affected rather by a minor merger approaching the nucleus [70, Fig. 29]. Fraquelli et al. (2000) [34] note that gas in this extended emission shares the same kinematics as the rest of the galaxy outside the FOV, suggesting the presence of an AGN outflow with a collimating axis oriented at an angle $\leq 30^\circ$ with respect to the galactic plane; this small angle is required to allow the nuclear radiation to intercept the gas in the disk and to allow a direct line-of-sight to the BLR. They propose an opening angle larger than 60° for the ionizing radiation cone. This suggestion is consistent with my results: both [N II] and [S II] share the same kinematic PA ($\approx 120^\circ$), $\approx 10^\circ$ less

than the kinematic PA of Hα, Hβ, [O I], and [O III] ($\approx$130 °). Besides, the offset in the kinematic centers of Hα, Hβ, [O I] and [O III] are closest to the direction of the ionization cone [158°, 34]. Both facts allow us to infer that the high-ionization emission lines are more affected by this cone, while [N II] and [S II] appear to be dominantly from gas rotating in the galactic plane, and following a rotation curve similar to that of the stars (Fig. 3.8).

The PV diagrams (Fig. 3.10) of [O III] and Hα clearly show a second velocity component $\sim$150 km s^{-1} to the red. Its contribution is most significant in the inner arcsecond and is the reason why the single Gaussian fit gives velocities redder than the expectation of pure rotation in the nucleus (see Fig. 3.7). The equivalent PV diagrams for [O I] and Hβ (not shown) are also consistent with the presence of the second higher velocity component, but double Gaussians could not be rigorously fit to these profiles due to their relative faintness, especially at distances $\gtrsim$ 1.5" from the nucleus (see Fig. 3.1). Further, both [O I] and Hβ (not shown) show the same asymmetries as [O III] and Hα in their velocity maps derived from a single Gaussian fit (Fig. 3.7).

Given that the appearance of the velocity fields (PAs, velocity ranges, rotation curves) of the low-velocity component of [O III] and Hα (middle panels of Fig. 3.12) are very similar to those derived from [N II] in the same region, this component is interpreted as emission from gas in the galactic disk, rotating in the same way as the [N II]-emitting gas and the stars. Only the negative velocities in [O III], reached very close to the nucleus (from -75 km s^{-1} to -120 km s^{-1}), can be attributed to an outflow approaching us.

The high-velocity component of both these lines shows a very different velocity field, with values that exceed the 200 km s^{-1}. Then, it can be concluded that the high-velocity component corresponds to the bright gas within the cone, ionized by the AGN. Given that velocities larger than 100 km s^{-1} are typically observed in outflows instead of inflows in nearby galaxies, the most plausible explanation is that the high-velocity component is gas entrained by the AGN outflow at an angle i greater than zero, located behind the plane of the sky from the line-of-sight, and thus redshifted to the observer. Why would the gas be preferably seen on the side farthest from the ionization cone (redshifted

to us) rather than on the near side (which would be blueshifted)? The explanation lies in the illumination of the NLR clouds by the AGN: on the far side of the cone in ESO 362-G18 is seen the side of the gas cloud which is illuminated by the AGN, while on the near side is seen primarily the "dark" side of the NLR clouds [see, e.g., 59]. The low and high velocity components in ESO 362-G18 are reminiscent of the case in NGC 4151 [106], with the difference that in NGC 4151 the high-velocity component corresponds to gas illuminated by a symmetric bicone, extending both in front and behind of the galactic plane, while in ESO 362-G18 only the gas in front the galactic disk, illuminated by a single ionization cone, is seen.

Agís-González et al. (2014) [1] have estimated an inner accretion disk inclination of $53° \pm 5°$; on the other hand, using the ratio between the minor and major photometric axis from Winkler (1997) [115], Fraquelli et al. (2000) [34] derived a galactic disk inclination of $\approx 37°$. Therefore, it can be suggested a picture for ESO 362-G18 were the ionization cone has an inclination angle $i \sim 8° \pm 5°$ with respect to the plane of the sky with a half-opening angle of 45° - also suggested by Agís-González et al. (2014) [1] - in such a way that the cone intersects with the galactic disk in the SE direction, illuminating gas receding from the line-of-sight due to the outflow. Only very close to the nucleus (see Fig. 3.12, middle top panel), where the [O III] gas is entrained by the approaching side of the cone in a small region corresponding to the thickness of the disk or bulge of the galaxy, do is seen blueshifted gas. This proposed configuration for the nuclear region in ESO 362-G18 is shown schematically in Fig. 4.1.

For both [O III] and Hα, the highest dispersion values are predominantly reached in the low-velocity component (Fig. 3.13), which is interpreted as gas rotation in the galactic disk. Only the central region of the high-velocity component (the outflow component) in [O III] shows dispersions higher than 100 km s^{-1}, which can be interpreted as coming from the approaching side of the outflow where the outflow is still within the galactic disk. The value of $\sigma_{H\alpha}$ of the outflow component is very sensitive to the subtraction of the broad emission in Hα, which was done before the two Gaussian fit, so the large dispersion values ($\sim$0.8" SE from the nucleus) should be taken with some reserve since this is po-

tentially due to confusion with the broad emission. Then, it can only be deduced that the decrease of $\sigma_{[O\,iii]}$ and $\sigma_{H\alpha}$ in the outflow component is due to its partial occultation by the galactic disk.

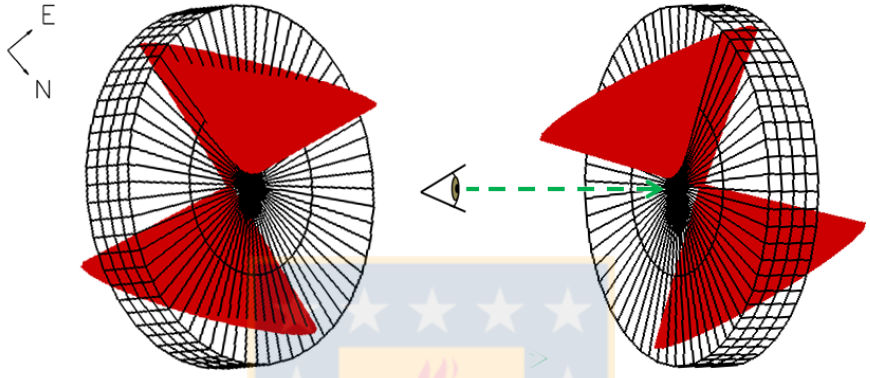

Figure 4.1: The proposed configuration for the nuclear region of ESO 362-G18 (see Chapter 4) where the galactic disk is shown both from my perspective (left; in the same orientation as the datacube) and in profile (right). The SE (top) ionization cone is towards us and intersects the galaxy disk primarily behind the plane of the sky, thus generating the high velocity (redshifted) component of [O III] and Hα. It also intersects the galaxy disk in front of the plane of the sky, but only in a very small region close to the nucleus, producing the greatest blueshift seen in the low velocity component of [O III]. On the other hand, the NW (bottom) ionization cone, if it does exist, is almost always hidden by the galactic disk for the line-of-sight. From this work.

4.1 Feeding versus Feedback

It can be estimate the mass outflow rate as the ratio between the mass of the outflowing gas and the dynamical time at the nucleus, M_g/t_d. The gas mass is given by:

$$M_g = N_e m_p V f \tag{4.1}$$

where N_e is the electron density, m_p is the mass of the proton, V is the volume of the region where the outflow is detected -that will be fix as 0."34 around the nucleus (i.e., within the seeing)-, and f is the filling factor. The filling factor can be estimated from:

$$L_{H\alpha} \approx f N_e^2 j_{H\alpha}(T) V \tag{4.2}$$

where $j_{H\alpha}$(T)=3.3534×10^{-25} erg cm^{-3}s^{-1} [79] and $L_{H\alpha}$ is the Hα luminosity emitted within the volume V. Substituting equation (2) into equation (1) it follows that:

$$M_g = \frac{M_p L_{H\alpha}}{N_e j_{H\alpha}(T)} \tag{4.3}$$

In Chapter 4, it was concluded that the high-velocity component detected both in [O III] and Hα are produced by the emission of clouds in front of the galactic disk, which is entrained by the AGN outflow. Therefore, the Hα luminosity will be estimated from the highest velocity component, yielding $L_\alpha = 1.5 \times 10^{40}$ erg s^{-1}, considering a luminosity distance to ESO 362-G18 of 52.1 Mpc (from NED). On the other hand, N_e is assumed as the mean value of 2453 cm^{-3} within the inner 0."34 from the nucleus. Taking into account all those values, the value of the ionized gas mass is 1.5×10^4 M$_\odot$ for the outflow component.

The dynamical time t_d can be estimated as the ratio between the radius where the outflow is considered (0."34 $\approx$ 84pc) and the mean deprojected velocity of the outflow ($\sim$394 km s^{-1}). This gives a t_d of $\sim 2 \times 10^5$ years. Finally, the mass outflow rate $\dot{M}$ is 0.074 M$_\odot$ yr^{-1}. It should be noted that this $\dot{M}$ is only a lower limit, since it corresponds only to the outflowing mass associated with the ionized side of the clouds. Additionally, if a biconical outflow is considered, assuming that most of the far side of the bicone is hidden by the galactic disk, the $\dot{M}$ can be twice the calculated value, that is, $\dot{M} \approx 0.15$ M$_\odot$ yr^{-1}, in agreement with others $\dot{M}$ observed in nearby galaxies [7, 59, 72]

It can be compare the mass outflow rate with the mass accretion rate required to feed the supermassive black hole $\dot{M}_{acc}$, which can be estimated as:

$$\dot{M}_{acc} = \frac{L_{bol}}{\eta c^2} \tag{4.4}$$

where c is the speed of light and L_{bol} is the bolometric luminosity. Using the L_{bol} estimated by [1] of 1.3×10^{44} erg s^{-1}, the resulting mass accretion rate is 2.2×10^{-2} M$_\odot$ yr^{-1}, with the assumption that the radiative efficiency, η, is 0.1, the typical value derived from Shakura-Sunyaev accretion models onto a non-rotating black hole [100]. Therefore, the $\dot{M}_{acc}$ is ~ 7 times fewer than the mass outflow rate. This is consistent with previous works in nearby galaxies [7, 72] and indicate that most of the observed outflowing gas is mass entrained by the surrounding interstellar medium [104, 114].

Although this value of $\dot{M}_{acc}$ is larger than $10^{-4.5}$ M$_\odot$ yr^{-1} [26, Fig. 10], large twists in the gas kinematic or important misalignments between the gas and the stellar kinematics are not observed. Thus, the nuclear activity in ESO 362-G18 may be related to major mergers in the past [45] that do not leave current disturbances in its kinematics, rather than perturbations in the ionized gas or misalignments between the stellar and gas rotations [26]. The posited minor merger observed in the acquisition image (Fig. 3.1) produces no discernible changes in the gas or stellar kinematics observed.

Considering the galactic disk and broad components of Hα, the total ionized gas mass within $\sim$84 pc of the nucleus is $\sim 3.3 \times 10^5$ M$_\odot$. Assuming that a small percentage ($\sim 5\%$) of all available gas would be accreted by the SMBH, infall velocities of ~ 2 km s^{-1} in this gas would be required to feed both the outflow and SMBH accretion.

4.2 The Kinetic Power

Considering an outflow bicone, with a mass outflow rate ($\dot{M}_{out}$) of 0.148 M$_\odot$ yr^{-1}, the kinetic power ($\dot{E}_{out}$) can be obtained using the following expression:

$$\dot{E}_{out} = \frac{1}{2}\dot{M}_{out}(v_{max}^2 + 3\sigma^2)$$

where v and σ are the average velocity and velocity dispersion of the outflowing gas, respectively. Taking these values from the nuclear region ($\leqslant$ 0."34) of the outflow component in Hα, v = 394 km s^{-1} and σ = 32 km s^{-1}; then the kinetic power of $\dot{E}_{out} = 9.2 \times 10^{39}$ erg s^{-1} was derived.

With the aim to measure the effect (feedback) of the ionized gas outflow on the galactic bulge, the kinetic power was compared with the accretion luminosity ($L_{bol} = 1.3 \times 10^{44}$ erg s^{-1}), obtaining a value of $\dot{E}_{out}/L_{bol} = 7 \times 10^{-5}$. This is at the lower end of the range (10^{-4} – 5×10^{-2}) found by Müller-Sánchez et al. (2011) [72] in a sample of six galaxies. The lower ratio obtained here could be attributed to large uncertainties in the velocity dispersion (σ_{inst} = 75 km s^{-1}) and the bolometric correction used to calculate L$_{bol}$ from L_X(2-10 keV) in Agís-González et al. (2014) [1]. This correction can vary widely (between 4 and 110) [e.g. 61, Figs. 7 and 8].

Chapter 5

SUMMARY

The gaseous and stellar kinematics of the inner 0.7 × 1.2 kpc^2 of the nearby Seyfert 1.5 galaxy ESO 362-G18 is observed using optical spectra (4092-7338 Å) from the GMOS integral field spectrograph on the Gemini South telescope, which allows the detection of a number of prominent emission lines: H$\beta\lambda$4861, [O III]$\lambda\lambda$4959,5007, Hα+[N II] $\lambda\lambda$6548,6583 and [S II]$\lambda\lambda$6716,6731. A variety of IDL and Python programs was employed to analyze these lines and obtain spatially resolved radial velocities, velocity dispersions and fluxes at a spatial resolution of ∼167 pc and a spectral resolution of 75 km s^{-1}. The main results of this paper are as follows.

- The Hα and [O III] lines clearly show double-peaked emission lines near the nucleus and to the SE. Two Gaussian fits are used to separate these profiles into two kinematic components: a low-velocity component and a high-velocity component.

- The stars, the [N II] and [S II] emission lines, and the low-velocity component of Hα and [O III] lines, typically have radial velocities between -80 km s^{-1} and 70 km s^{-1}, and have very similar rotation patterns, so all of these are interpreted as originated in the rotating galactic disk.

- The high-velocity component of Hα and [O III] reach values in excess of 200 km s^{-1} with respect to the systemic velocity and it

is argued that these spectral components originate from gas outflowing within the AGN radiation cone. A toy model is presented to explain why this gas is preferentially redshifted to the line of sight, except at the nucleus where blueshifted [O III] emission from the outflow traces the region where the outflow is still breaking out of the galactic disk. The effects of AGN ionization has been previously observed, showing a fan-shaped morphology with an extension of ≈ 10" to the southeast in emission-line and excitation maps.

- The assumption that the outflow component is behind the plane of the sky is also motivated by the flux observed in [O III]: while the disk component presents the highest fluxes in most of the FOV, the outflow component exceeds it in the nuclear region, where the highest blueshift velocities are reached. This difference is consistent with attenuation from the galactic disk except very close to the nucleus, where the approaching side of the cone can be seen.

- The structure of the nuclear region of ESO 362-G18 presents spiral arms in a trailing pattern, which are increasingly fainter as the nucleus is reached. Considering the linear scale of the observations, it is posited that the unusual dust morphology is a result of instabilities produced near the inner Lindblad resonance, which is expected within the inner 1.6kpc. The presence of the dust structures also supports the hypothesis of Simões Lopes et al. (2007) [102], that the presence of dust is a necessary condition for the nuclear activity in AGNs.

- While morphologically there is evidence that ESO 362-G18 is participating in a minor merger, any effect of this in the stellar or gas kinematics is not found, within the relatively small FOV.

- Using the Hα luminosity, a lower limit for the mass outflow rate $\dot{M}$ of 0.074 $M_{\odot}$ yr^{-1} is estimated. This value will double if a biconical outflow is assumed. Further, the value calculated is likely a lower limit to the outflow mass and rate, since the H_{α} luminosity used to calculate the outflow gas mass only represents the fraction of the NLR gas clouds illuminated by the AGN, rather than all of

the outflowing NLR gas. In any case, my estimated outflow rate is significantly higher than the accretion rate necessary to sustain the AGN bolometric luminosity, that is, $\dot{M}_{acc} \sim 2.2 \times 10^{-2}$ M yr^{-1}.

Bibliography

[1] B. Agís-González, G. Miniutti, E. Kara, A. C. Fabian, M. Sanfrutos, G. Risaliti, S. Bianchi, N. L. Strotjohann, R. D. Saxton, and M. L. Parker, *Black hole spin and size of the X-ray-emitting region(s) in the Seyfert 1.5 galaxy ESO 362-G18*, mnras, 443 (2014), pp. 2862–2873.

[2] M. P. Agüro, *Kinematics and Dynamics of Spiral Galaxies*, PhD thesis, Observatorio Astronómico de Córdoba ¡EMAIL¿mpaguero@oac.uncor.edu¡/EMAIL¿, 2010.

[3] H. Akaike, *A New Look at the Statistical Model Identification*, IEEE Transactions on Automatic Control, 19 (1974), pp. 716–723.

[4] R. Antonucci, *Unified models for active galactic nuclei and quasars*, araa, 31 (1993), pp. 473–521.

[5] R. R. J. Antonucci and J. S. Miller, *Spectropolarimetry and the nature of NGC 1068*, apj, 297 (1985), pp. 621–632.

[6] J. A. Baldwin, M. M. Phillips, and R. Terlevich, *Classification parameters for the emission-line spectra of extragalactic objects*, pasp, 93 (1981), pp. 5–19.

[7] F. K. B. Barbosa, T. Storchi-Bergmann, R. Cid Fernandes, C. Winge, and H. Schmitt, *Gemini/GMOS IFU gas velocity 'tomography' of the narrow line region of nearby active galaxies*, mnras, 396 (2009), pp. 2–18.

[8] M. C. Begelman, R. D. Blandford, and M. J. Rees, *Theory of extragalactic radio sources*, Reviews of Modern Physics, 56 (1984), pp. 255–351.

[9] N. Bennert, B. Jungwiert, S. Komossa, M. Haas, and R. Chini, *Size and properties of the narrow-line region in Seyfert-1 galaxies from spatially-resolved optical spectroscopy*, aap, 459 (2006), pp. 55–69.

[10] F. Bertola, D. Bettoni, J. Danziger, E. Sadler, L. Sparke, and T. de Zeeuw, *Testing the gravitational field in elliptical galaxies - NGC 5077*, apj, 373 (1991), pp. 369–390.

[11] G. S. Bisnovatyi-Kogan and R. V. E. Lovelace, *Advective accretion disks and related problems including magnetic fields*, nar, 45 (2001), pp. 663–742.

[12] A. Bosma, *21-cm line studies of spiral galaxies. II. The distribution and kinematics of neutral hydrogen in spiral galaxies of various morphological types.*, aj, 86 (1981), pp. 1825–1846.

[13] A. H. Bridle, D. H. Hough, C. J. Lonsdale, J. O. Burns, and R. A. Laing, *Deep VLA imaging of twelve extended 3CR quasars*, aj, 108 (1994), pp. 766–820.

[14] A. H. Bridle and R. A. Perley, *Extragalactic Radio Jets*, araa, 22 (1984), pp. 319–358.

[15] M. Cappellari and Y. Copin, *Adaptive spatial binning of integral-field spectroscopic data using Voronoi tessellations*, mnras, 342 (2003), pp. 345–354.

[16] M. Cappellari and E. Emsellem, *Parametric Recovery of Line-of-Sight Velocity Distributions from Absorption-Line Spectra of Galaxies via Penalized Likelihood*, pasp, 116 (2004), pp. 138–147.

[17] R. Cid Fernandes, G. Stasińska, M. S. Schlickmann, A. Mateus, N. Vale Asari, W. Schoenell, and L. Sodré,

Alternative diagnostic diagrams and the 'forgotten' population of weak line galaxies in the SDSS, mnras, 403 (2010), pp. 1036–1053.

[18] F. Combes, S. García-Burillo, V. Casasola, L. K. Hunt, M. Krips, A. J. Baker, F. Boone, A. Eckart, I. Marquez, R. Neri, E. Schinnerer, and L. J. Tacconi, *ALMA reveals the feeding of the Seyfert 1 nucleus in NGC 1566*, aap, 565 (2014), p. A97.

[19] d. A. d. G. Corwin, H. G. Jr., *Southern Galaxy Catalogue. A Catalogue of 5481 Galaxies South of Declination -17 Degrees Found on 1.2m U.K. Schmidt IIIa-J Plates*, 1985.

[20] D. M. Crenshaw, S. B. Kraemer, and J. R. Gabel, *The Host Galaxies of Narrow-Line Seyfert 1 Galaxies: Evidence for Bar-Driven Fueling*, aj, 126 (2003), pp. 1690–1698.

[21] G. Cresci, A. Marconi, S. Zibetti, G. Risaliti, S. Carniani, F. Mannucci, A. Gallazzi, R. Maiolino, B. Balmaverde, M. Brusa, A. Capetti, C. Cicone, C. Feruglio, J. Bland-Hawthorn, T. Nagao, E. Oliva, M. Salvato, E. Sani, P. Tozzi, T. Urrutia, and G. Venturi, *The MAGNUM survey: positive feedback in the nuclear region of NGC 5643 suggested by MUSE*, aap, 582 (2015), p. A63.

[22] R. I. Davies, W. Maciejewski, E. K. S. Hicks, E. Emsellem, P. Erwin, L. Burtscher, G. Dumas, M. Lin, M. A. Malkan, F. Müller-Sánchez, G. Orban de Xivry, D. J. Rosario, A. Schnorr-Müller, and A. Tran, *Fueling Active Galactic Nuclei. II. Spatially Resolved Molecular Inflows and Outflows*, apj, 792 (2014), p. 101.

[23] R. I. Davies, J. Thomas, R. Genzel, F. Müller Sánchez, L. J. Tacconi, A. Sternberg, F. Eisenhauer, R. Abuter, R. Saglia, and R. Bender, *The Star-forming Torus and Stellar Dynamical Black Hole Mass in the Seyfert 1 Nucleus of NGC 3227*, apj, 646 (2006), pp. 754–773.

[24] G. de Vaucouleurs, A. de Vaucouleurs, H. G. Corwin, Jr., R. J. Buta, G. Paturel, and P. Fouqué, *Third Reference Catalogue of Bright Galaxies. Volume I: Explanations and references. Volume II: Data for galaxies between 0^h and 12^h. Volume III: Data for galaxies between 12^h and 24^h.*, 1991.

[25] T. Di Matteo, V. Springel, and L. Hernquist, *Energy input from quasars regulates the growth and activity of black holes and their host galaxies*, nat, 433 (2005), pp. 604–607.

[26] G. Dumas, C. G. Mundell, E. Emsellem, and N. M. Nagar, *Central kiloparsec of Seyfert and inactive host galaxies: a comparison of two-dimensional stellar and gaseous kinematics*, mnras, 379 (2007), pp. 1249–1278.

[27] E. Emsellem, K. Fathi, H. Wozniak, P. Ferruit, C. G. Mundell, and E. Schinnerer, *Gas and stellar dynamics in NGC 1068: probing the galactic gravitational potential*, mnras, 365 (2006), pp. 367–384.

[28] E. Emsellem, D. Greusard, F. Combes, D. Friedli, S. Leon, E. Pécontal, and H. Wozniak, *Dynamics of embedded bars and the connection with AGN. I. ISAAC/VLT stellar kinematics*, aap, 368 (2001), pp. 52–63.

[29] P. Englmaier and I. Shlosman, *Dynamical Decoupling of Nested Bars: Self-gravitating Gaseous Nuclear Bars*, apjl, 617 (2004), pp. L115–L118.

[30] P. Erwin and L. S. Sparke, *A WIYN Survey of Early-Type Barred Galaxies: Double Bars and Central Structures*, in Galaxy Dynamics - A Rutgers Symposium, D. R. Merritt, M. Valluri, and J. A. Sellwood, eds., vol. 182 of Astronomical Society of the Pacific Conference Series, Aug. 1999.

[31] A. C. Fabian, *Observational Evidence of Active Galactic Nuclei Feedback*, araa, 50 (2012), pp. 455–489.

[32] K. Fathi, T. Storchi-Bergmann, R. A. Riffel, C. Winge, D. J. Axon, A. Robinson, A. Capetti, and A. Marconi, *Streaming Motions toward the Supermassive Black Hole in NGC 1097*, apjl, 641 (2006), pp. L25–L28.

[33] T. C. Fischer, D. M. Crenshaw, S. B. Kraemer, and H. R. Schmitt, *Determining Inclinations of Active Galactic Nuclei via their Narrow-line Region Kinematics. I. Observational Results*, apjs, 209 (2013), p. 1.

[34] H. A. Fraquelli, T. Storchi-Bergmann, and L. Binette, *The Extended Narrow-Line Region of the Seyfert 1 Galaxy ESO 362-G18 versus That of the Seyfert 2 Galaxy ESO 362-G8*, apj, 532 (2000), pp. 867–882.

[35] B. García-Lorenzo, E. Mediavilla, S. Arribas, and C. del Burgo, *Evidence of Two Kinematically Different Stellar Systems in NGC 1068*, apjl, 483 (1997), pp. L99–L102.

[36] O. E. Gerhard, *Line-of-sight velocity profiles in spherical galaxies: breaking the degeneracy between anisotropy and mass.*, mnras, 265 (1993), p. 213.

[37] G. Gimeno, K. Roth, K. Chiboucas, P. Hibon, L. Boucher, J. White, M. Rippa, K. Labrie, J. Turner, K. Hanna, M. Lazo, G. Pérez, R. Rogers, R. Rojas, V. Placco, and R. Murowinski, *On-sky commissioning of hamamatsu ccds in gmos-s*, 2016.

[38] J. E. Greene and L. C. Ho, *A Comparison of Stellar and Gaseous Kinematics in the Nuclei of Active Galaxies*, apj, 627 (2005), pp. 721–732.

[39] J. E. Greene, N. L. Zakamska, and P. S. Smith, *A Spectacular Outflow in an Obscured Quasar*, apj, 746 (2012), p. 86.

[40] K. Gültekin, D. O. Richstone, K. Gebhardt, T. R. Lauer, S. Tremaine, M. C. Aller, R. Bender, A. Dressler, S. M.

Faber, A. V. Filippenko, R. Green, L. C. Ho, J. Kormendy, J. Magorrian, J. Pinkney, and C. Siopis, *The M-sigma and M-L Relations in Galactic Bulges, and Determinations of Their Intrinsic Scatter*, apj, 698 (2009), pp. 198–221.

[41] N. Häring and H.-W. Rix, *On the Black Hole Mass-Bulge Mass Relation*, apjl, 604 (2004), pp. L89–L92.

[42] L. Hernquist, *Tidal triggering of starbursts and nuclear activity in galaxies*, nat, 340 (1989), pp. 687–691.

[43] L. C. Ho, *Nuclear activity in nearby galaxies*, Annual Review of Astronomy and Astrophysics, 46 (2008), pp. 475–539.

[44] L. C. Ho, A. V. Filippenko, and W. L. W. Sargent, *A Search for "Dwarf" Seyfert Nuclei. III. Spectroscopic Parameters and Properties of the Host Galaxies*, apjs, 112 (1997), pp. 315–390.

[45] P. F. Hopkins, K. Bundy, D. Croton, L. Hernquist, D. Keres, S. Khochfar, K. Stewart, A. Wetzel, and J. D. Younger, *Mergers and Bulge Formation in ΛCDM: Which Mergers Matter?*, apj, 715 (2010), pp. 202–229.

[46] P. F. Hopkins and M. Elvis, *Quasar feedback: more bang for your buck*, mnras, 401 (2010), pp. 7–14.

[47] M. Karouzos, M. Im, M. Trichas, T. Goto, M. Malkan, A. Ruiz, Y. Jeon, J. H. Kim, H. M. Lee, S. J. Kim, N. Oi, H. Matsuhara, T. Takagi, K. Murata, T. Wada, K. Wada, H. Shim, H. Hanami, S. Serjeant, G. J. White, C. Pearson, and Y. Ohyama, *A Tale of Two Feedbacks: Star Formation in the Host Galaxies of Radio AGNs*, apj, 784 (2014), p. 137.

[48] G. Kauffmann, T. M. Heckman, C. Tremonti, J. Brinchmann, S. Charlot, S. D. M. White, S. E. Ridgway, J. Brinkmann, M. Fukugita, P. B. Hall, Ž. Ivezić, G. T. Richards, and D. P. Schneider, *The host galaxies of active galactic nuclei*, mnras, 346 (2003), pp. 1055–1077.

[49] L. J. Kewley, C. Maier, K. Yabe, K. Ohta, M. Akiyama, M. A. Dopita, and T. Yuan, *The Cosmic BPT Diagram: Confronting Theory with Observations*, apjl, 774 (2013), p. L10.

[50] J. H. Knapen, *Gravitationally Induced Inflow in Starbursts and Agn*, apss, 295 (2005), pp. 85–94.

[51] J. H. Knapen, I. Shlosman, C. H. Heller, R. J. Rand, J. E. Beckman, and M. Rozas, *Kinematics of Ionized and Molecular Hydrogen in the Core of M100*, apj, 528 (2000), pp. 219–235.

[52] J. Kormendy and K. Gebhardt, *Supermassive black holes in galactic nuclei*, in 20th Texas Symposium on relativistic astrophysics, J. C. Wheeler and H. Martel, eds., vol. 586 of American Institute of Physics Conference Series, Oct. 2001, pp. 363–381.

[53] D. Krajnović, M. Cappellari, P. T. de Zeeuw, and Y. Copin, *Kinemetry: a generalization of photometry to the higher moments of the line-of-sight velocity distribution*, mnras, 366 (2006), pp. 787–802.

[54] S. Laine, I. Shlosman, J. H. Knapen, and R. F. Peletier, *Nested and Single Bars in Seyfert and Non-Seyfert Galaxies*, apj, 567 (2002), pp. 97–117.

[55] S. Laine, R. P. van der Marel, J. Rossa, J. E. Hibbard, J. C. Mihos, T. Böker, and A. I. Zabludoff, *A Hubble Space Telescope WFPC2 Investigation of the Nuclear Morphology in the Toomre Sequence of Merging Galaxies*, aj, 126 (2003), pp. 2717–2739.

[56] E. Laurikainen, H. Salo, and R. Buta, *Comparison of Bar Strengths and Fractions of Bars in Active and Nonactive Galaxies*, apj, 607 (2004), pp. 103–124.

[57] D. Lena, *Reduction of Integral Field Spectroscopic Data from the Gemini Multi-Object Spectrograph (a commented example)*, ArXiv e-prints, (2014).

[58] ——, *Aspects of Supermassive Black Hole Growth in Nearby Active Galactic Nuclei*, PhD thesis, Rochester Institute of Technology, 2015.

[59] D. Lena, A. Robinson, T. Storchi-Bergman, A. Schnorr-Müller, T. Seelig, R. A. Riffel, N. M. Nagar, G. S. Couto, and L. Shadler, *The Complex Gas Kinematics in the Nucleus of the Seyfert 2 Galaxy NGC 1386: Rotation, Outflows, and Inflows*, apj, 806 (2015), p. 84.

[60] M.-Y. Lin, R. I. Davies, L. Burtscher, A. Contursi, R. Genzel, E. González-Alfonso, J. Graciá-Carpio, A. Janssen, D. Lutz, G. Orban de Xivry, D. Rosario, A. Schnorr-Müller, A. Sternberg, E. Sturm, and L. Tacconi, *Thick discs, and an outflow, of dense gas in the nuclei of nearby Seyfert galaxies*, mnras, 458 (2016), pp. 1375–1392.

[61] E. Lusso, A. Comastri, B. D. Simmons, M. Mignoli, G. Zamorani, C. Vignali, M. Brusa, F. Shankar, D. Lutz, J. R. Trump, R. Maiolino, R. Gilli, M. Bolzonella, S. Puccetti, M. Salvato, C. D. Impey, F. Civano, M. Elvis, V. Mainieri, J. D. Silverman, A. M. Koekemoer, A. Bongiorno, A. Merloni, S. Berta, E. Le Floc'h, B. Magnelli, F. Pozzi, and L. Riguccini, *Bolometric luminosities and Eddington ratios of X-ray selected active galactic nuclei in the XMM-COSMOS survey*, mnras, 425 (2012), pp. 623–640.

[62] D. Lynden-Bell, *Galactic Nuclei as Collapsed Old Quasars*, nat, 223 (1969), pp. 690–694.

[63] W. Maciejewski, *Nuclear spirals in galaxies: gas response to an asymmetric potential - I. Linear theory*, mnras, 354 (2004), pp. 883–891.

[64] ——, *Nuclear spirals in galaxies: gas response to an asymmetric potential - II. Hydrodynamical models*, mnras, 354 (2004), pp. 892–904.

[65] D. Makarov, P. Prugniel, N. Terekhova, H. Courtois, and I. Vauglin, *HyperLEDA. III. The catalogue of extragalactic distances*, aap, 570 (2014), p. A13.

[66] M. A. Malkan, V. Gorjian, and R. Tam, *A Hubble Space Telescope Imaging Survey of Nearby Active Galactic Nuclei*, apjs, 117 (1998), pp. 25–88.

[67] P. Martini, M. W. Regan, J. S. Mulchaey, and R. W. Pogge, *Circumnuclear Dust in Nearby Active and Inactive Galaxies. II. Bars, Nuclear Spirals, and the Fueling of Active Galactic Nuclei*, apj, 589 (2003), pp. 774–782.

[68] E. Mediavilla and S. Arribas, *Evidence for an offset active nucleus in the Seyfert galaxy NGC3227*, nat, 365 (1993), pp. 420–422.

[69] R. Morganti, J. Holt, L. Saripalli, T. A. Oosterloo, and C. N. Tadhunter, *IC 5063: AGN driven outflow of warm and cold gas*, aap, 476 (2007), pp. 735–743.

[70] J. S. Mulchaey, A. S. Wilson, and Z. Tsvetanov, *An Emission-Line Imaging Survey of Early-Type Seyfert Galaxies. I. The Observations*, apjs, 102 (1996), p. 309.

[71] F. Müller Sánchez, R. I. Davies, F. Eisenhauer, L. J. Tacconi, R. Genzel, and A. Sternberg, *SINFONI adaptive optics integral field spectroscopy of the Circinus Galaxy*, aap, 454 (2006), pp. 481–492.

[72] F. Müller-Sánchez, M. A. Prieto, E. K. S. Hicks, H. Vives-Arias, R. I. Davies, M. Malkan, L. J. Tacconi, and R. Genzel, *Outflows from Active Galactic Nuclei: Kinematics of the Narrow-line and Coronal-line Regions in Seyfert Galaxies*, apj, 739 (2011), p. 69.

[73] T. Murayama and Y. Taniguchi, *Where is the coronal line region in active galactic nuclei?*, The Astrophysical Journal Letters, 497 (1998), p. L9.

[74] N. M. Nagar, A. S. Wilson, J. S. Mulchaey, and J. F. Gallimore, *Radio Structures of Seyfert Galaxies. VIII. A Distance- and Magnitude-Limited Sample of Early-Type Galaxies*, apjs, 120 (1999), pp. 209–245.

[75] N. P. H. Nesvadba, M. Polletta, M. D. Lehnert, J. Bergeron, C. De Breuck, G. Lagache, and A. Omont, *The dynamics of the ionized and molecular interstellar medium in powerful obscured quasars at z greater than 3.5*, mnras, 415 (2011), pp. 2359–2372.

[76] H. Netzer, *Revisiting the Unified Model of Active Galactic Nuclei*, araa, 53 (2015), pp. 365–408.

[77] R. Nevin, J. Comerford, F. Müller-Sánchez, R. Barrows, and M. Cooper, *The Origin of Double-peaked Narrow Lines in Active Galactic Nuclei. II. Kinematic Classifications for the Population at z greater than 0.1*, apj, 832 (2016), p. 67.

[78] D. E. Osterbrock, *Spectrophotometry of Seyfert 1 galaxies*, apj, 215 (1977), pp. 733–745.

[79] ——, *Astrophysics of gaseous nebulae and active galactic nuclei*, 1989.

[80] D. E. Osterbrock and G. J. Ferland, *Astrophysics of gaseous nebulae and active galactic nuclei*, 2006.

[81] D. E. Osterbrock and R. W. Pogge, *The spectra of narrow-line Seyfert 1 galaxies*, apj, 297 (1985), pp. 166–176.

[82] G. Paturel, G. Theureau, L. Bottinelli, L. Gouguenheim, N. Coudreau-Durand, N. Hallet, and C. Petit, *HYPERLEDA. II. The homogenized HI data*, aap, 412 (2003), pp. 57–67.

[83] B. M. Peterson, *An Introduction to Active Galactic Nuclei*, Cambridge Univ. Press, (1997).

[84] R. W. Pogge and P. Martini, *Hubble Space Telescope Imaging of the Circumnuclear Environments of the CfA Seyfert Galaxies: Nuclear Spirals and Fueling*, apj, 569 (2002), pp. 624–640.

[85] A. E. Reines, J. E. Greene, and M. Geha, *Dwarf Galaxies with Optical Signatures of Active Massive Black Holes*, apj, 775 (2013), p. 116.

[86] J. Reunanen, J. K. Kotilainen, and M. A. Prieto, *Near-infrared spectroscopy of nearby Seyfert galaxies II. Molecular content and coronal emission*, mnras, 343 (2003), pp. 192–208.

[87] R. Riffel, A. Rodríguez-Ardila, and M. G. Pastoriza, *A 0.8-2.4 μm spectral atlas of active galactic nuclei*, aap, 457 (2006), pp. 61–70.

[88] R. A. Riffel, *profit: a new alternative for emission-line profile fitting*, apss, 327 (2010), pp. 239–244.

[89] R. A. Riffel and T. Storchi-Bergmann, *Compact molecular disc and ionized gas outflows within 350 pc of the active nucleus of Mrk 1066*, mnras, 411 (2011), pp. 469–486.

[90] R. A. Riffel, T. Storchi-Bergmann, and C. Winge, *Feeding versus feedback in AGNs from near-infrared IFU observations: the case of Mrk 79*, mnras, 430 (2013), pp. 2249–2261.

[91] R. A. Riffel, T. Storchi-Bergmann, C. Winge, P. J. McGregor, T. Beck, and H. Schmitt, *Mapping of molecular gas inflow towards the Seyfert nucleus of NGC4051 using Gemini NIFS*, mnras, 385 (2008), pp. 1129–1142.

[92] A. Rodríguez-Ardila, M. G. Pastoriza, and C. J. Donzelli, *Visible and Near-Infrared Spectroscopy of Seyfert 1 and Narrow-Line Seyfert 1 Galaxies*, apjs, 126 (2000), pp. 63–78.

[93] A. Rodríguez-Ardila, S. M. Viegas, M. G. Pastoriza, and L. Prato, *Near-Infrared Coronal Lines in Narrow-Line Seyfert 1 Galaxies*, apj, 579 (2002), pp. 214–226.

[94] D. S. N. Rupke and S. Veilleux, *Integral Field Spectroscopy of Massive, Kiloparsec-scale Outflows in the Infrared-luminous QSO Mrk 231*, apjl, 729 (2011), p. L27.

[95] P. Sánchez-Blázquez, R. F. Peletier, J. Jiménez-Vicente, N. Cardiel, A. J. Cenarro, J. Falcón-Barroso, J. Gorgas, S. Selam, and A. Vazdekis, *Medium-resolution Isaac Newton Telescope library of empirical spectra*, mnras, 371 (2006), pp. 703–718.

[96] M. Sarzi, J. Falcón-Barroso, R. L. Davies, R. Bacon, M. Bureau, M. Cappellari, P. T. de Zeeuw, E. Emsellem, K. Fathi, D. Krajnović, H. Kuntschner, R. M. McDermid, and R. F. Peletier, *The SAURON project - V. Integral-field emission-line kinematics of 48 elliptical and lenticular galaxies*, mnras, 366 (2006), pp. 1151–1200.

[97] A. Schnorr-Müller, T. Storchi-Bergmann, F. Ferrari, and N. M. Nagar, *Gas inflows towards the nucleus of the Seyfert 2 galaxy NGC 1667*, mnras, 466 (2017), pp. 4370–4380.

[98] A. Schnorr-Müller, T. Storchi-Bergmann, N. M. Nagar, A. Robinson, D. Lena, R. A. Riffel, and G. S. Couto, *Feeding and feedback in the inner kiloparsec of the active galaxy NGC 2110*, mnras, 437 (2014), pp. 1708–1724.

[99] A. Schnorr Müller, T. Storchi-Bergmann, R. A. Riffel, F. Ferrari, J. E. Steiner, D. J. Axon, and A. Robinson, *Gas streaming motions towards the nucleus of M81*, mnras, 413 (2011), pp. 149–161.

[100] N. I. Shakura and R. A. Sunyaev, *Black Holes in Binary Systems: Observational Appearances*, in X- and Gamma-Ray Astronomy, H. Bradt and R. Giacconi, eds., vol. 55 of IAU Symposium, 1973, p. 155.

[101] I. Shlosman, M. C. Begelman, and J. Frank, *The fuelling of active galactic nuclei*, nat, 345 (1990), pp. 679–686.

[102] R. D. Simões Lopes, T. Storchi-Bergmann, M. de Fátima Saraiva, and P. Martini, *A Strong Correlation between Circumnuclear Dust and Black Hole Accretion in Early-Type Galaxies*, apj, 655 (2007), pp. 718–734.

[103] Y. Sofue and V. Rubin, *Rotation Curves of Spiral Galaxies*, araa, 39 (2001), pp. 137–174.

[104] T. Storchi-Bergmann, *Active Galactic Nuclei at the Smallest Scales: Infall and Obscuration*, in Resolving The Future Of Astronomy With Long-Baseline Interferometry, M. J. Creech-Eakman, J. A. Guzik, and R. E. Stencel, eds., vol. 487 of Astronomical Society of the Pacific Conference Series, Sept. 2014, p. 199.

[105] T. Storchi-Bergmann, O. L. Dors, Jr., R. A. Riffel, K. Fathi, D. J. Axon, A. Robinson, A. Marconi, and G. Östlin, *Nuclear Spirals as Feeding Channels to the Supermassive Black Hole: The Case of the Galaxy NGC 6951*, apj, 670 (2007), pp. 959–967.

[106] T. Storchi-Bergmann, R. D. S. Lopes, P. J. McGregor, R. A. Riffel, T. Beck, and P. Martini, *Feeding versus feedback in NGC4151 probed with Gemini NIFS - II. Kinematics*, mnras, 402 (2010), pp. 819–835.

[107] E. Sturm, E. González-Alfonso, S. Veilleux, J. Fischer, J. Graciá-Carpio, S. Hailey-Dunsheath, A. Contursi, A. Poglitsch, A. Sternberg, R. Davies, R. Genzel, D. Lutz, L. Tacconi, A. Verma, R. Maiolino, and J. A. de Jong, *Massive Molecular Outflows and Negative Feedback in ULIRGs Observed by Herschel-PACS*, apjl, 733 (2011), p. L16.

[108] C. Tadhunter, *An introduction to active galactic nuclei: Classification and unification*, nar, 52 (2008), pp. 227–239.

[109] H. D. Tran, *The Unified Model and Evolution of Active Galaxies: Implications from a Spectropolarimetric Study*, apj, 583 (2003), pp. 632–648.

[110] E. Treister, K. Schawinski, C. M. Urry, and B. D. Simmons, *Major Galaxy Mergers Only Trigger the Most Luminous Active Galactic Nuclei*, apjl, 758 (2012), p. L39.

[111] Z. I. Tsvetanov and A. R. Petrosian, *H II Region Populations in Seyfert Galaxies. I. Database*, apjs, 101 (1995), p. 287.

[112] P. C. van der Kruit and R. J. Allen, *The kinematics of spiral and irregular galaxies*, araa, 16 (1978), pp. 103–139.

[113] R. P. van der Marel and M. Franx, *A new method for the identification of non-Gaussian line profiles in elliptical galaxies*, apj, 407 (1993), pp. 525–539.

[114] S. Veilleux, G. Cecil, and J. Bland-Hawthorn, *Galactic Winds*, araa, 43 (2005), pp. 769–826.

[115] H. Winkler, *The extinction, flux distribution and luminosity of Seyfert 1 nuclei derived from UBV(RI)$_C$ aperture photometry*, mnras, 292 (1997), p. 273.

[116] X.-B. Wu, F. Wang, X. Fan, W. Yi, W. Zuo, F. Bian, L. Jiang, I. D. McGreer, R. Wang, J. Yang, Q. Yang, D. Thompson, and Y. Beletsky, *An ultraluminous quasar with a twelve-billion-solar-mass black hole at redshift 6.30*, nat, 518 (2015), pp. 512–515.